6. Site 1145[1]

Shipboard Scientific Party[2]

BACKGROUND AND OBJECTIVES

The primary objectives of Site 1145 (SCS-2) on the northern margin of the South China Sea were to (1) recover a continuous sequence of deep-water, hemipelagic sediments to reconstruct the middle Pliocene to Pleistocene/Holocene paleomonsoon history; (2) establish whether the South China Sea records an intensification of the winter monsoon during the Pliocene–Pleistocene, coincident with the development of loess in China, and whether the summer monsoon is intensifying or weakening during the Pliocene–Pleistocene; and (3) reconstruct (in conjunction with Site 1144) the water-mass depth gradients and ventilation history of the South China Sea during the Quaternary.

Site 1145 (SCS-2) is located at 19°35.04′N, 117°37.86′E (Fig. F9, p. 53, in the "Leg 184 Summary" chapter). The site lies downslope from Site 1144 at a water depth of ~3175.5 m, which is below the sill depth of the Bashi Strait (2600 m). Based on piston core data, sedimentation rates were expected to be ~100 to ~200 m/m.y. or about one-half to one-third of those at Site 1144.

Site 1145 is located at shotpoint 4704 (11:10) on the seismic Line SO95-10 (Figs. F5, p. 17, and F10, p. 23, both in the "Seismic Stratigraphy" chapter) on the lower of a series of terraces that form the continental slope off southern China. The thick, conformable sediments extend almost 1 second below seafloor (sbsf) to a strong wavy reflector, presumed to be prerift sediments. Using the interval velocities provided by Hamburg and Tongji Universities, this two-way time is equivalent to ~760 m of sediment cover. The 200 meters below seafloor (mbsf) penetration expected at Site 1145 should reach 0.28 sbsf. The seismic structure within the upper 200 mbsf contains an upper zone of multiple (about six) strong reflectors (0–0.12 sbsf) and a lower, more diffuse zone (0.12–0.28 sbsf) that is divided by a prominent reflector at ~0.21 sbsf (Fig. F6, p. 18, in the "Seismic Stratigraphy" chapter). The northwest-

southeast dip line (SO95-10) reveals sediments that are generally smooth and slightly onlapping onto the continental slope from the adjacent deep basin. The *JOIDES Resolution* 3.5-kHz data and SO-95 PARASOUND data (Sarnthein et al., 1994) reveal relatively smooth, parallel, conformable sediment cover with no distinct surface features (Fig. F7, p. 20, in the "Seismic Stratigraphy" chapter).

We expected Site 1145 to have hemipelagic clays, similar to Site 1144 but with less carbonate and organic carbon. We predicted that the multiple advanced hydraulic piston corer (APC) holes at Site 1145 would provide a high-quality spliced record from the late Pliocene to Pleistocene (Holocene). These records should allow us to apply a wide range of monsoonal and paleoceanographic proxies to reconstruct the orbital-scale climate changes in the Quaternary and late Pliocene and the water-mass and ventilation changes across the Bashi Strait sill, which is the only deep-water connection between the Pacific and the South China Sea.

Given scientific priorities, time constraints, and shipboard operational limitations, we adjusted our plan to triple APC core to refusal and to deepen all three holes to 200 mbsf with the extended core barrel (XCB) if the APC did not reach 200 mbsf.

OPERATIONS

Site 1145 (Proposed Site SCS-2)

The short voyage to Site 1145 (proposed site SCS-2) covered the 31 nmi at an average speed of 10.3 kt. The beacon was dropped on precise Global Positioning System coordinates at 1950 hr on 18 March. The corrected precision depth recorder referenced to the dual elevator stool was 3194.4 m.

Hole 1145A

Hole 1145A was spudded with the APC at 0245 hr on 19 March. The seafloor depth was inferred from the recovery of the first core as 3187.1 m. Piston coring advanced to 125.0 mbsf with an average recovery of 100.1%. The cores were oriented starting with Core 4H. During piston coring, heat-flow measurements were obtained at 30, 58, 96, and 200 mbsf. The last measurement was made with the Davis-Villinger temperature probe. A temperature gradient of 90°C/km was calculated from these data (see "Physical Properties," p. 15). The hole was deepened with the XCB to the target depth of 200.0 mbsf. The XCB average recovery was 81.9%; the average recovery for this hole was 93.3% (Tables T1, T2, both also in ASCII format). Only a trace amount of methane was detected in the cores (see "Organic Geochemistry," p. 11).

Hole 1145B

The vessel was offset 10 m west of Hole 1145A, and Hole 1145B was spudded with the APC at 0145 hr on 20 March. The seafloor depth, inferred from the recovery of the first core, was 3185.9 m. Piston coring advanced to 120.6 mbsf with an average recovery of 99.5%. The cores were oriented starting with Core 3H. The hole was deepened to the target depth of 200.0 mbsf with the XCB. The XCB-cored portion of the

T1. Site 1145 coring summary, **p. 48.**

T2. Site 1145 coring summary by section, **p. 50.**

hole averaged only 74.8% because of zero recovery in one of the core barrels (20X). The average recovery for the hole was 89.7% (Tables T1, T2).

Hole 1145C

The vessel was offset 10 m west of Hole 1145B, and Hole 1145C was spudded with the APC at 2015 hr on 20 March. The seafloor depth was inferred to be 3187.9 m. Piston coring advanced to 121.6 mbsf with an average recovery of 101.4%. The cores were oriented starting with Core 3H. The hole was deepened to 198.4 mbsf with the XCB; the average XCB recovery was 86.0%. The average recovery for the hole was 95.4% (Tables T1, T2).

The total core recovered at this site was 555.2 m, or 92.8% of the cored interval of 598.1 m. The bit was at the rotary table by 1630 hr on 21 March, and the vessel began the 78-nmi voyage to Site 1146.

COMPOSITE SECTION

We built a continuous meters composite depth (mcd) scale and a splice (as defined in the "Composite Section," p. 3, in the "Explanatory Notes" chapter) that range from the top of Core 184-1145C-1H to the bottom of Section 21X-7. The splice and the mcd scale extend continuously from 0.0 to 132.58 mcd. Extension of a continuous splice below this interval was precluded by incomplete core recovery and alignment of core gaps. However, as described below and in the "Composite Section," p. 3, in the "Explanatory Notes" chapter, we were able to construct a discontinuous ("floating") mcd scale and splice for the interval spanning 139.8 to 210.0 mcd.

The mcd scale and the splice are based on the stratigraphic correlation of whole-core multisensor track (MST) and split-core color spectral reflectance (CSR) data (lightness, L*) collected at 4- to 5-cm intervals (see "Physical Properties," p. 15, for details). From the MST, we used magnetic susceptibility (MS), gamma-ray attenuation (GRA) bulk density, and natural gamma radiation (NGR) data. These data, and the splice constructed from them, are presented on the mcd scale in Figures F1, F2, F3, and F4 (also as Synergy Software KaleidaGraph plots and Microsoft Excel data files [see the "Supplementary Materials" contents list]; the spliced records are also available in ASCII format). The depth offsets that comprise the mcd scale are given in Table T3 (also in ASCII format). The splice tie points (Table T4, also in ASCII format) should be used as a guide for detailed postcruise sampling.

Magnetic susceptibility data were the most useful stratigraphic tool for correlation at this site; the MS profiles for the three holes are extremely similar, even at very fine (centimeter) scales.

We constructed the mcd scale by assuming that the uppermost sediment (the "mudline") in Core 184-1145C-1H was the sediment/water interface. This core, the "anchor" in the composite depth scale, has the same depth on both the mbsf and mcd scales. We correlated downhole from this anchor, core by core, until we reached 132 mcd. At this point, aligned core gaps prevented further downhole construction of the continuous mcd scale and splice.

Although the cores below 132 mcd could not be tied directly to the continuous composite depth scale and thus the splice, they could be correlated with each other. We were able to place these cores on a dis-

F1. Smoothed/correlated MS data and splice, p. 19.
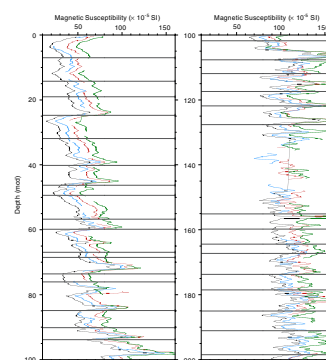
F2. Smoothed/correlated NGR data and splice, p. 21.
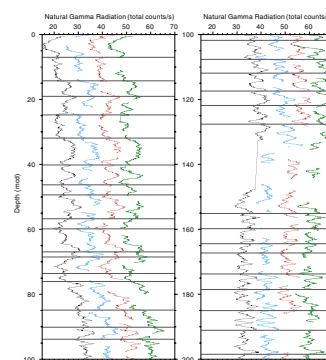
F3. Smoothed/correlated GRA data and splice, p. 23.
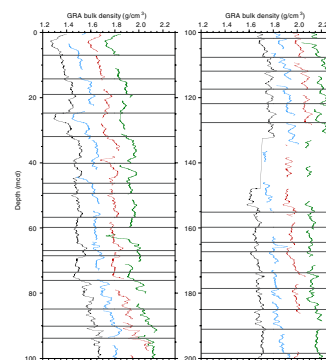
continuous composite depth scale. This "floating" scale is not tied to the overlying mcd scale (and thus back to the mudline). Instead, the positions of the cores are adjusted such that correlative features match. We chose Core 184-1145B-16X as the top of the floating splice. The depth of this core on the mcd scale is based on the overlying continuous mcd scale. Cores at similar depths from adjacent holes were mapped to Core 184-1145B-16X; correlation then progressed downhole, as in the construction of the continuous mcd scale.

LITHOSTRATIGRAPHY

Lithologic Units

Unit I (0–212.65 mcd)

Interval: Cores 184-1145A-1H through 22X; Cores 184-1145B-1H through 22X; Cores 184-1145C-1H through 21X
Depth: 0–200.00 mbsf (Hole 1145A); 0–200.00 mbsf (Hole 1145B); 0–198.10 mbsf (Hole 1145C)
Age: late Pliocene to Holocene

The section at Site 1145 mainly consists of clay, and only one sedimentary unit is assigned to the sediments at this site (Fig. F5). In addition to clay minerals, the upper part (0–75 mbsf; 0–85.6 mcd) is characterized by small amounts (<10%) of biogenic silica, mainly in the form of radiolarians, diatoms, sponge spicules, and silicoflagellates. Below 40 mbsf (42.9 mcd), the percentage of calcareous nannofossils increases slightly (<10%), although the abundance of planktonic foraminifers remains moderate.

A red-brown oxidized layer (mudline) is observed in interval 184-1145A-1H-1, 0–15 cm (0–0.15 mbsf; 0–0.15 mcd), and consists of clay with radiolarians, sponge spicules as long as 1 cm, and small amounts of nannofossils. This layer is intensely bioturbated, and a dark brown manganese-rich redox horizon is observed at its base. Soupy greenish gray clay with foraminifers, nannofossils, and radiolarians dominates below this horizon.

Carbonate content estimated from smear slides varies within the sediment but is rarely higher than 10%, except within some of the lighter gray intervals (Table T5). The visually identified light carbonate-rich layers seen in the cores were also detected with color reflectance data collected by spectrophotometer (Fig. F5). The latter data set was effective in showing that carbonate content varied over a broader zone than noted by the naked eye.

Carbonate-Rich Intervals

Slightly lighter intervals, with higher carbonate content, are observed throughout the entire interval. We systematically recorded these intervals only for Hole 1145C (Table T5). Internal sedimentary features in the light layers include abundant visible foraminifers, common green clay layers (typically 1–3 cm thick), and slightly yellowish gray patches, which probably represent traces of bioturbation. The higher carbonate content of the light layers results in a stiffer clay, which often shows a rough surface caused by the cutting wire. A typical example of these light gray carbonate-rich intervals is a mottled nanno-

F4. Smoothed/correlated L* values from the CSR data and splice, p. 25.
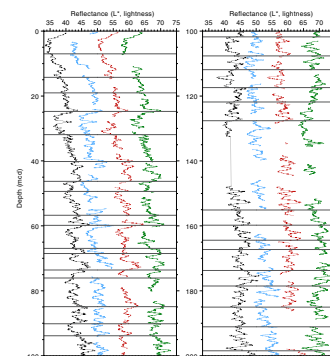
T3. Composite depths for Site 1145, p. 51.

T4. Site 1145 splice tie points, p. 52.

F5. Site 1145 section summary, p. 27.
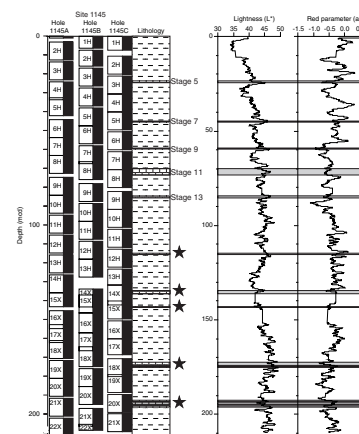
T5. Intervals of lighter colored sediment, p. 53.

fossil ooze bed (more than 50% nannofossil observed in smear slides) with gradational top and basal contacts, occurring in interval 184-1145A-7H-4, 43–123 cm (59.43–60.23 mcd [Fig. F5]). This bed is not a turbidite deposit; instead, its character suggests a short-term increase in carbonate production or a decrease in carbonate dissolution. It may correspond to isotopic Stage 9.

Green Layers and Mottles

Green layers and less distinct green mottles, which resemble the green clay layers observed at Site 1143, occur frequently in the upper part of the drilled sequence, principally above ~170 mcd. They are characterized by stiff clay and have a lower water content and a faster *P*-wave velocity.

Bioturbation

Bioturbation is intense throughout the cored interval. The sediment is generally completely homogenized, and individual burrows are observed only rarely. Exceptions are the pyrite-filled burrows, which occur at a frequency of about one to two per section throughout the drilled intervals, commencing at ~28.5 mcd. Large pyrite-filled burrows reach several centimeters in length and up to 2 cm in diameter. Remineralization of former organic carbon-rich sediments is also expressed by pyrite layers. For example, a fecal pellet horizon is fossilized in interval 184-1145A-15X-1, 2–5 cm (136.3 mcd; Fig. F6).

Fossils

Shell fragments and complete tests of pteropods are commonly observed in the upper part (above 73.6 mcd) of the recovered section. A unique feature of Site 1145 is the presence of several complete echinoderms, which were only cut and fragmented by core splitting. Some echinoderm fragments are remineralized by pyrite (e.g., Section 184-1145A-7H-CC, 43 cm; 64.43 mcd). Biogenic silica represented by radiolarians, sponge spicules, diatoms, and silicoflagellates is abundant and represents an important part of the biogenic fraction in the upper part of the holes. Biogenic silica progressively decreases in abundance and is seldom observed below 81 mcd.

Three wood fragments were found at Site 1145. Samples were taken for detailed shore-based analysis. Wood is preserved at intervals 184-1145A-13H-4, 4–6 cm (120.6 mcd), 184-1145B-1H-1, 10–11 cm (0.1 mcd), and 184-1145C-9H-2, 100–101 cm (85.5 mcd). The largest wood fragment is more than 4 cm long and almost 1 cm in diameter (Fig. F7).

Siliciclastic and Volcaniclastic Layers

Slightly darker intervals that have gradational contacts with the dominant sediment are noted at intervals 184-1145B-3H-5, 60–63 cm (23.7 mcd), and 3H-6, 33–37 cm (24.9 mcd). These beds contain increased amounts of pyrite and volcanic glass and may correspond to volcanic ash layers, homogenized by bioturbation. At Section 184-1145A-5H-2, 66 cm (34.9 mcd), a pyrite-stained volcanic pumice clast 1.2 cm long is observed. A small number of cores contain fresh angular volcanic glass shards within burrows, as well as dispersed ash within the sediment (Fig. F8). Volcanic ash represents a volumetrically insignifi-

F6. Fecal pellet accumulation replaced by pyrite, **p. 28.**
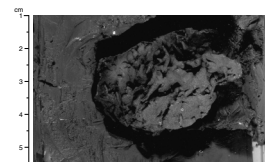
F7. Wood debris, **p. 29.**
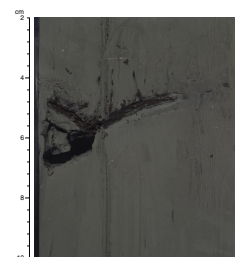
F8. Volcanic ash layer dispersed in burrows, **p. 30.**
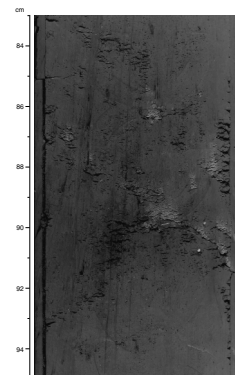
cant proportion of the total sequence. Because of intense bioturbation, the correlation of ash layers from hole to hole is not always possible (Table T6).

An unusual nodular cemented silt layer with a sharp basal contact is observed in intervals 184-1145B-16X-6, 93–99 cm (156.13–156.19 mcd), and 184-1145C-16X-4, 25–29 cm (156.25–156.29 mcd). This layer may be a diagenetically altered silty turbidite layer or a strongly altered volcanic ash.

Foraminifer Turbidites

Thin foraminifer turbidites occur at Site 1145 but are rare. The best example is observed in interval 184-1145B-18X-7, 49 cm, through 18X-CC, 2 cm (175.19–175.24 mcd). This ~5-cm-thick, normally graded turbidite has a sharp bottom contact and consists almost entirely of planktonic foraminiferal tests.

Composition of the Terrigenous Component

X-ray diffraction of randomly packed bulk sediment samples demonstrates no long-term changes in the terrigenous mineral composition within the sediment at this site (Fig. F9). The most notable changes are the increase in carbonate and decrease in plagioclase below 160 mcd in the light gray carbonate-rich layers.

Discussion

The most striking features of the sedimentary section recovered at Site 1145 are light carbonate-rich clay layers of ~0.5- to 4-m thickness. The contacts of these layers are generally gradational, and the transition zone is only a few centimeters long in most cases. These observations closely correspond to the spectrophotometer measurements that indicate changes of ~8% of the total lightness (L* parameter). These intervals are also characterized by more common layers, mottles, and patches of green clay and have higher contents of foraminifers and calcareous nannoplankton. The higher density of green layers and bioturbation (mottles and patches) within these intervals are an indication of increased biogenic activity in the sedimentary environment.

We interpret the light intervals as representing deposition during relative sea-level highstands, when Site 1145 was largely protected from terrigenous flux by broad flooded shelves. This interpretation agrees with the biostratigraphic data, which allows us to tentatively place the first five important light intervals in the interglacial isotope Stages 5, 7, 9, 11, and 13 (Fig. F5). Relationships between lightness, carbonate content, and relative sea level have also been reported in this area by Sarnthein et al. (1994). Changes in the lysocline depth could also explain some variations in the carbonate (lightness) content. The present-day lysocline is located between 3000 and 3200 m. Because Site 1145 was drilled at 3200 meters below sea level, this location is especially sensitive to any change of sea level, seawater properties, and primary productivity. Several additional light layers are observed below 84.5 mcd in Hole 1145C (Fig. F5; Table T5). However, the identification of these layers becomes more problematic with depth, as the average sediment composition becomes more carbonate rich and the contrast between dark and light layers decreases. Because correlation with the color
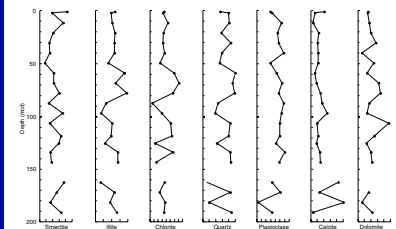
reflectance curve becomes increasingly difficult, we do not attempt to correlate these layers with isotope stages.

BIOSTRATIGRAPHY

Calcareous Nannofossils

Site 1145 yielded common to abundant, poor to moderately well-preserved upper Pleistocene through upper Pliocene calcareous nanno-fossils. Nannofossil biostratigraphy at this site is based on a detailed study of Hole 1145A (Tables T7, T8). All nannofossil bioevents are confirmed in Holes 1145B and 1145C without significant variations. Nannofossil preservation and abundance varies at different levels, indicating changes in calcite dissolution or dilution by other sediment components. Calcite dissolution is evident in all samples as indicated by etching on the rim of placoliths and disappearance of central structures.

Emiliania huxleyi dominates the nannofossil assemblages in the top 10 m of sediments, but its abundance decreases significantly below 22.3 mcd. Therefore, the first occurrence (FO) of "*E. huxleyi* increase" is tentatively drawn at 11.9 mcd. The next three Pleistocene biohorizons, the FO of *E. huxleyi,* the last occurrence (LO) of *Pseudoemiliania lacunosa,* and the LO of *Calcidiscus macintyrei,* occur in the correct order of succession between 53.0 and 152.8 mcd. The interval 115.0–126.0 mcd was assigned to the *Gephyrocapsa* (small) acme Zone based on the significant reduction in abundance of large and medium-sized *Gephyrocapsa* spp. Medium-sized (>4 mm) *Gephyrocapsa* spp. were not observed at Site 1145 below the LO of *C. macintyrei.* Therefore, the Pleistocene/Pliocene boundary can only be constrained by the LO of *C. macintyrei* (152.8 mcd) and the next lower biohorizon, the LO of *Discoaster brouweri* (164.9 mcd).

The LO of *D. brouweri,* the LO of *Discoaster pentaradiatus,* and the LO of *Discoaster tamalis* were recorded in the correct order of succession in the bottom 48 m in Hole 1145A. The LO of *Discoaster surculus* was not resolved at this site because of the low sampling resolution. Calcareous nannofossil preservation deteriorates significantly in the lowermost 48 m at Site 1145, which indicates severe calcite dissolution. This suggests that Site 1145 was probably below the nannofossil lysocline during the late Pliocene.

Planktonic Foraminifers

Planktonic foraminifers were also examined in all core-catcher samples from Hole 1145A and in selected core-catcher samples from Holes 1145B and 1145C. The soft clay in the samples of this site was easily removed by soaking in a warm Calgon and hydrogen peroxide solution and then washing through a 150-µm sieve. Site 1145 yields a moderate abundance of planktonic foraminifers, although their preservation degrades from good to poor downsection. This preservation was documented by an increase in fragmentation (Le and Shackleton, 1992) and a decrease of pteropod abundance with depth (see Fig. F10). In general, the upper part of Hole 1145A (above ~90 mcd) has good preservation as indicated by low fragmentation and relatively high ratios of preserved pteropods to planktonic foraminifers. Because this site is located within the modern lysocline of the South China Sea, its carbonate dissolution

T7. Summary of biohorizons, p. 55.

T8. Calcareous nannofossil checklist, p. 56.

F10. Age-depth plot, p. 32.
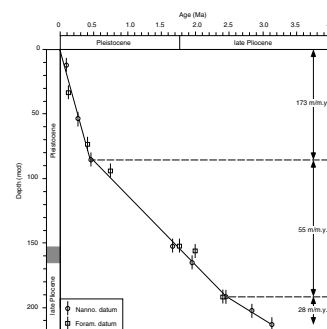
should be very sensitive to the changes in lysocline depth. Therefore, the high fragmentation (>15%) at ~140 mcd and below ~165 may indicate that this site was below the lysocline at that time (see Fig. **F10**).

The planktonic foraminiferal biostratigraphy for Site 1145 is based on Holes 1145A and 1145B (see Table **T9** for details). The relatively high sedimentation rates at Site 1145 and the depth of the drilled section limit the number of biohorizons used to date the cores. The LO of *Globigerinoides fistulosus* (1.77 Ma) was used to mark the Pleistocene/Pliocene boundary (152.8 mcd), whereas the FO of *Globorotalia truncatulinoides* marked the bottom of Zone N22 (155.5 mcd) (Blow, 1969). Within Zone N22, the LO (0.12 Ma; Thompson et al., 1979) and the FO (0.40 Ma; Li, 1997) of pink *Globigerinoides ruber*, as well as the FO of *Globorotalia crassaformis* (0.75 Ma), served as three biostratigraphic control points (Table **T9**). The bottom of the site (212.5 mcd) was constrained by the LO of *Sphaeroidinellopsis seminulina* (3.12 Ma) and the FO of *Globorotalia tosaensis* (3.35 Ma), placing it in Zone N21.

Benthic Foraminifers

Site 1145 yields rare to few deep-sea benthic foraminifers, but the ratio of benthic to planktonic foraminifers increases greatly in the lower part of Hole 1145A, possibly because of increased carbonate dissolution. The proportion of species indicative of high organic carbon flux (e.g., *Globobulimina* spp. and *Uvigerina peregrina*), is high above ~85 mcd and then decreases downhole. This corresponds well to changes in the group abundance of siliceous microfossils (such as radiolarians and diatoms) (Fig. **F11**) and in the organic carbon content in Hole 1145A. It also indicates that productivity decreases downhole. The LO of *Stilostomella* was observed at 94.3 mcd, placing this depth at 0.75 Ma for the latitude of this site (Schönfeld, 1996).

Summary

At Site 1145, both planktonic foraminifers and calcareous nannofossils are common to abundant, although planktonic foraminifer preservation degraded from good to poor downsection and the nannofossils were occasionally to commonly reworked. Benthic foraminifers are generally few in number.

An age-depth plot of the three fossil groups shows that the biohorizons generally agree with each other (Fig. **F11**). The age of the oldest sediments recovered at Site 1145 is ~3.12–3.35 Ma. The sedimentation rate at Site 1145, calculated based on biostratigraphic data (Table **T7;** Fig. **F11**), is 173 m/m.y. after 0.46 Ma, 28 m/m.y. before 2.0 Ma, and 55 m/m.y. in between.

PALEOMAGNETISM

Shipboard paleomagnetic measurements for Holes 1145A, 1145B, and 1145C consisted of long-core measurements of natural remanent magnetization (NRM) at intervals of 8 cm before and after alternating field (AF) demagnetization, usually up to 20 mT, carried out on the archive halves of all APC and XCB cores. In addition, 116 discrete samples were collected from the working halves of Hole 1145A (APC and XCB cores), at a spacing of one sample per section (1.5 m). These samples were subjected to progressive AF demagnetization with 10 steps up

T9. Planktonic foraminifer checklist, **p. 57.**

F11. Downhole changes, **p. 33.**
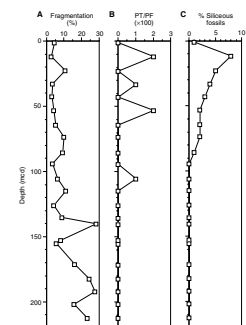
to 50 mT. Cores 184-1145A-3H through 14H, 184-1145B-3H through 13H, and 184-1145C-3H through 13H were oriented using the Tensor tool.

Hole 1145A

The nonmagnetic cutting shoe was used with a standard core barrel on every second core starting with Core 184-1145A-5H. Long-core measurements were carried out at 8-cm intervals with only one AF demagnetization step at 20 mT.

The direction of the NRM (after demagnetization at 20 mT and correction using the Tensor tool data where available) is shown in Figure F12. Above 93.0 mcd, declination oscillates around 0° and inclination around ~38°, which is the value expected for a geocentered dipole field at this latitude. The amplitude of the fluctuations in declination and inclination is consistent with the secular variation of the geomagnetic field. At 93.0 mcd, the Brunhes/Matuyama boundary is clearly identified by a sudden swing of the declination to 180°. Farther downcore at 110.6 mcd, a change to northerly declinations marks the upper Jaramillo transition. The lower Jaramillo transition is situated at ~116.1 mcd.

Farther downcore, the overprint resulting from the coring process increases and is not completely removed by the one-step demagnetization procedure imposed by the rate of core flow. This increasing contribution of the overprint to the magnetization is revealed by high positive inclinations, particularly at the reversals: although inclinations do display changes of ~70° as expected at this latitude, these changes are centered around 40°, not 0°. Also, the scatter of the inclinations is increased in XCB cores. Because the overprint was not completely removed by the long-core AF demagnetization, the occurrence of the Olduvai Event was obscured. Long-core measurements did reveal the Gauss/Matuyama boundary at 190 mcd as a jump of the inclination from ~25° to ~45° (no declination is obtained from XCB cores).

Demagnetization of the discrete samples proved to be more efficient in removing the overprint, probably because of the combined effect of reduced overprint in the center of the core together with the more careful demagnetizing procedure (10 steps of demagnetization up to 50 mT). Examples of demagnetization diagrams clearly show that a reverse (I = <0°) primary component is recovered after demagnetization (Fig. F13). Inclinations obtained from discrete samples are reported in Figure F12 as open squares. The discrete sample results are quite consistent with long-core measurements, and the Olduvai Event is clearly revealed from 154.6 to 164.7 mcd. Further, the inclinations around the Gauss/Matuyama boundary are closer to their expected values.

From 190 mcd to the bottom of Hole 1145A, some discrete samples appear to be heavily overprinted (I = >50°), but two samples yield unequivocal reverse inclinations. This indicates that the upper Kaena reversal (3.04 Ma) may have been reached in this hole at 210 mcd. If this hypothesis is correct, the change in sedimentation rate from 37.3 m/m.y. to 28.0 m/m.y. at 2.6 Ma suggested by biostratigraphic results (see "Biostratigraphy," p. 7) might not exist.

Comparison with the magnetic polarity time scale yields the age-depth relationship shown in Table T10.

F12. Declination and inclination for Hole 1145A, 0–210 mcd, p. 34.
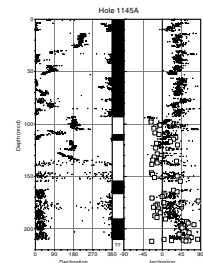
F13. Representative AF demagnetization diagrams from discrete samples, p. 35.
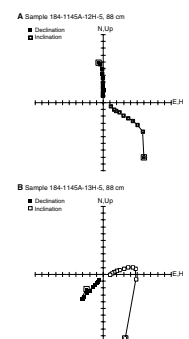
T10. Age-depth relationship from the magnetic polarity time scale, p. 58.

Hole 1145B

Only long-core measurements were made on cores from Hole 1145B at an interval of 8 cm and one demagnetization step at 20 mT. As discussed above in "Hole 1145A," p. 9, one demagnetization step at this level is not sufficient to fully demagnetize the overprint, particularly in XCB cores.

The Brunhes/Matuyama boundary was found at a depth of 93.1 mcd. Farther downcore, the upper Jaramillo transition is placed at 110.5 mcd, whereas the lower Jaramillo transition is situated at a depth of 115.26 mcd. In Hole 1145B, the Olduvai is obscured by overprinting in the XCB cores.

Hole 1145C

Long-core measurements for Hole 1145C were conducted as in Hole 1145B. The only difference was for XCB cores, where two steps of demagnetization at 20 and 30 mT were done to reduce the overprint.

The Brunhes/Matuyama boundary was found at a depth of 92.8 mcd. The upper Jaramillo is located at a depth of 110.3 mcd; the lower Jaramillo, at 115.3 mcd. As in Holes 1145A and 1145B, the Olduvai was obscured by the overprint even at higher demagnetization levels.

SEDIMENTATION AND ACCUMULATION RATES

Because of the moderate to good preservation of calcareous microfossils and the lessened magnetic overprint of the APC cores, both micropaleontological and paleomagnetic data can be used for chronostratigraphy. A total of 20 datum levels were found at Site 1145: six magnetic, seven calcareous nannofossil, six planktonic foraminifer, and one benthic foraminifer event (see Table T7; Fig. F12).

Figure F14 (also given as Synergy Software KaleidaGraph plots and Microsoft Excel data files [see the "Supplementary Materials" contents list]) shows the linear sedimentation rate and mass accumulation rate curves based on calculations described in "Sedimentation and Accumulation Rates," p. 13, in the "Explanatory Notes" chapter. The resultant average sedimentation rates decrease from 227 m/m.y. in the upper ~60 m to some 40 m/m.y. down to the bottom (Fig. F14B), a difference of almost one order of magnitude. When converted to mass accumulation rates, both carbonate and noncarbonate accumulations show the same decreasing trend downhole, with a small increase in the middle part of the sequence. Variations in accumulation rate are much more significant in the noncarbonate fraction. The rate was low in the Pliocene, averaging 4 g/cm^2/k.y., and then rose to 6 g/cm^2/k.y. in the early Pleistocene. After 0.8 Ma, the noncarbonate accumulation exhibited an almost threefold increase to 13 g/cm^2/k.y. in the last 0.26 Ma (Fig. F14; Table T11). Because this pattern of accumulation rate changes is common to other sites (e.g., Sites 1144 and 1146), its interpretation must involve basinwide, if not regional, events.

F14. Age-depth model, LSR, and MAR, p. 36.
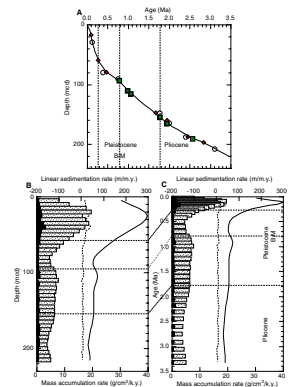
T11. Sedimentation and accumulation rates for selected intervals, p. 59.

ORGANIC GEOCHEMISTRY

Overview

Only trace amounts of methane (<16 ppmv) and no other hydrocarbon gases were detected in sediments at Site 1145. Carbonate concentrations were mostly low, between 3 and 19 wt%, in the upper 190 mcd. There is a marked increase at 170 mcd, and in the lower 170–210 mcd of the sediment section, carbonate represents as much as 30 wt%. Total organic carbon (TOC) obtained by difference calculation (total carbon [TC] – inorganic carbon [IC]) declined steadily from >1 wt% at the top of Hole 1145A to much lower concentrations (~0.2 wt%) at the base, consisting of organic matter (OM) with a lower organic C/N ratio (probably marine OM).

Inorganic Carbon

Three samples per core were analyzed for inorganic carbon content, and one sample per core for TC, total nitrogen (TN), and total sulfur (TS) content from Hole 1145A (Table T12). Carbonate varies from 3.2 to 30.5 wt%, with two distinct intervals apparent (Fig. F15A). The upper interval (0–170 mcd) contains sediments with lower carbonate content (average [AV] = 10.65 wt%; standard deviation [SD] = 3.40), with some notable excursions (e.g., Sections 184-1145A-5H-5, 17.5 wt%; 12H-3, 3.2 wt%). However, below 170 mcd, carbonate content and variability increase significantly (AV = 18.82 wt%; SD = 7.07), reaching a maximum in Core 184-1145A-31X, then declining to the base of Hole 1145A.

Organic Carbon

The TOC concentration by difference (TC – IC) was determined for one sample per core for Hole 1145A (Table T12). It decreases from 1 wt% at the top of the hole to ~0.25 wt% from 0 to 130 mcd; below this level, values remain near 0.25 wt% to the bottom of the hole. Little correlation is observed between organic and inorganic carbon, and the decrease in TOC in the upper interval is independent of carbonate abundance (Fig. F15B).

Sulfur

Sulfur values vary between <0.02 and 0.36 wt%, with higher values paired with higher TOC values, mostly from the top of Hole 1145A down to Core 184-1145A-12H (Table T12). The very low values (<0.02 wt%) probably result from the small physical size of the carbonate samples (as opposed to a channel or composite sample representing the full section length) and from the localization of S in pyrite-filled burrows. Such burrows are reported (see "Lithostratigraphy," p. 4) in the lower cores of Hole 1145A, where these values are observed. The S analyses with very low values (<0.02 wt%) were made with a new reaction column, which produced a small S peak that apparently was below the integration limit of the instrument software. A blank (tin crucible with V_2O_5) run in the same set showed no S peak.
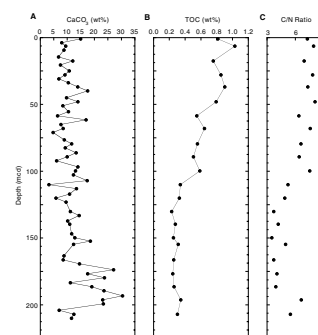
Organic Matter Characterization

Geochemical analysis of the sediments from Hole 1145A allows some characterization of the organic matter. As at previous sites on this leg (see "Organic Geochemistry," p. 18, in the "Site 1143" chapter and "Organic Geochemistry," p. 13, in the "Site 1144" chapter) and during previous Ocean Drilling Program (ODP) legs (cf. Carter, McCave, Richter, Carter, et al., 1999), the C/N ratio data include some unreasonably low values, even for fresh marine OM. These data suggest a systematic error in either the TOC by difference calculation or N determination or, alternatively, a significant contribution from inorganic N (Table T12). However, the range of C/N values is informative and indicates that the residual OM in Hole 1145A is of a degraded, predominantly marine origin. A significant shift to lower C/N values occurs at 100 mcd, well below the depth of most of the TOC reduction as indicated by the profile of dissolved sulfate (Figs. F15C, F16C).

Average marine organic matter is characterized by the "Redfield" ratio of carbon to nitrogen (106:16), a requirement of phytoplankton cells (Redfield et al., 1982; Riebesell et al., 1993; Broecker and Peng, 1982), yielding an expected average C/N value of ~7. However, research suggests that carbon consumption, relative to nitrogen, may occur in coastal and deep-sea waters both greater than and less than that predicted. In the deep ocean, most nitrogen is cycled within the upper layers; production is driven by ammonia released from degrading plankton. Nitrogen in plankton is present in an average weight ratio of 100:20 (Romankevich, 1984). For certain plankton the C/N ratio decreases to near 4 (e.g., diatomaceous suspensions). During complete OM mineralization, N is liberated as ammonium salts, which may undergo further oxidation to free nitrogen, nitrite, and nitrate ions as a result of bacterial activity. In sediments containing predominantly clay, nitrogenous compounds may be preferentially preserved from bacterial metabolism as the major proportion is tightly sorbed by the mineral base of the sediment (Suess and Müller, 1980). The impact of differences in composition of clay minerals, and benthic enrichment of the OM by clays with nitrogenous compounds, appears small (Romankevich, 1984).

In summary, the low C/N values recorded at this site may be partly explained by the origin of the OM. However, the declining TOC values with depth may suggest a possible increased ammonium content during OM destruction; such an increase in inorganic nitrogen may well explain the lower C/N values observed.

Seven samples from above 100 mbsf containing >0.5 wt% TOC (by difference) were analyzed by Rock-Eval pyrolysis (Table T13). All samples yielded calculated TOC values ~30% lower than calculated by difference (TC – IC). All samples yielded T_{max} values <400°C, indicating immature organic matter as expected from the shallow burial depth and normal geothermal gradient (see "Physical Properties," p. 15). The exception is Sample 184-1145A-12H-3, 107–108 cm, with a higher T_{max}. However, the inflection point of the S_2 peak from which the T_{max} is determined is indistinct, and the peak temperature assignation is therefore not precise. The S_2 peak for Sample 184-1145A-12H-3, 107–108 cm, appears to be the same as the other samples from Hole 1145A. The production index appears anomalously high for all samples relative to the T_{max}. This suggests that S_1 values are also anomalously high and would be expected to increase—not decrease—with depth if there was thermogenic generation of hydrocarbons. Both hydrogen index (HI) and

F16. Interstitial water measurements, p. 38.
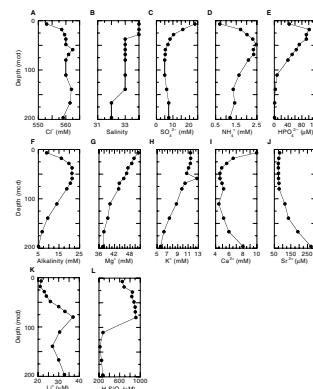
T13. Rock-Eval pyrolysis results, p. 61.

oxygen index (OI) values (see "Organic Geochemistry," p. 14, in the "Explanatory Notes" chapter) are less reliable for young, immature OM (Katz, 1983) but appear to be indicative of type III kerogen, lignin-rich of terrestrial origin or more oxidized marine OM. Nevertheless, the suggestion of highly oxidized residual organic material may well be applicable to such low HI and high OI values at this deep-water site, where the OM has sufficient time to be oxidized during settling through the water column to the sediment surface.

INORGANIC GEOCHEMISTRY

Inorganic chemical analyses were conducted on 12 interstitial water samples from Hole 1145A, squeezed from whole-round samples at a frequency of one per core in the first six cores and one every third core thereafter. Analytical methods are detailed in "Inorganic Geochemistry," p. 17, in the "Explanatory Notes" chapter. The concentrations of dissolved interstitial constituents are presented in Table T14, and the profiles with depth are shown in Figure F16. Interstitial water profiles at Site 1145 are characteristic of sediments in which sulfate reduction, alteration of volcanic material, and dissolution-recrystallization of biogenic minerals are the primary reactions controlling the concentrations of dissolved constituents.

Chloride and Salinity

Chloride (Cl^-) concentrations in interstitial waters are relatively constant, ranging from 553 to 561 mM (Fig. F16A; Table T14). A small increase in the Cl^- concentration occurs from 553 mM near the surface to 559 mM at 15.38 mbsf. Below this depth, Cl^- concentrations do not change significantly and are close to those of the seawater value (559 mM). Interstitial water salinities have a narrow range (32–34) (Fig. F16B; Table T14) and decrease slightly downhole.

Sulfate, Alkalinity, Ammonium, Phosphate, and pH

The sulfate (SO_4^{2-}), alkalinity, ammonium (NH_4^+), and phosphate (HPO_4^{2-}) profiles at Site 1145 show significant changes in the upper part of the sediment column (0 to ~100 mbsf), which are interpreted to be caused by the diagenesis of organic matter via sulfate reduction. Dissolved SO_4^{2-} concentrations decrease from 23.3 mM near the top of the core to 5.4 mM at 53.38 mbsf but never reach zero throughout the remainder of the hole. These SO_4^{2-} values indicate, as in Site 1143, that sulfate reduction is incomplete (Fig. F16C; Table T14) and that methanogenesis is a minor process in these sediments, which agrees with the low methane values detected in sediment (<14 ppmv) (see "Organic Geochemistry," p. 11). The removal of dissolved SO_4^{2-} ions from interstitial waters also causes the decrease in salinity observed from the top 0 to ~50 mbsf (Fig. F16B).

As expected, the interstitial water concentration of sulfate reduction products NH_4^+ and HPO_4^{2-} increases in the sulfate-reduction zone to a broad maximum of 2.5 mM at 43.4 mbsf and 101.4 mM at 15.4 mbsf (Fig. F16D, F16E; Table T14). Below these maxima, both NH_4^+ and HPO_4^{2-} concentrations decrease continuously to the base of the hole to the minima of 1.2 and 0.5 mM, respectively.

Alkalinity increases from 9.1 mM at 5 mbsf to a maximum of 21.3 mM at 34.4 mbsf and is nearly balanced stoichiometrically by a depletion of SO_4^{2-} over this depth range (Fig. F16F; Table T14). Below the sulfate reduction zone (0–50 mbsf), the alkalinity declines to a minimum of 5.1 mM at the base of the hole. The interstitial water pH remains in a narrow range (7.3–7.6) throughout the entire sedimentary column (Table T14).

Magnesium, Potassium, Calcium, and Strontium

Dissolved magnesium (Mg^{2+}) and potassium (K^+) concentrations decrease linearly with depth from near-seawater values at the top to a minimum of ~37.6 and 5.7 mM at the bottom of the hole, respectively (Fig. F16G, F16H; Table T14).

Dissolved calcium concentrations (Ca^{2+}) decrease downhole from near-seawater values at the surface (10 mM) to 4.6 mM at ~43.9 mbsf (Fig. F16I; Table T14), then remain low and relatively constant between 50 and 100 mbsf. Below this interval, the Ca^{2+} increases to a maximum of 8 mM near the bottom of the hole. The decrease of Ca^{2+} in the upper 100 mbsf of the hole most likely indicates that sulfate reduction and alkalinity production, which has an inverse relationship with Ca^{2+}, are promoting inorganic calcite precipitation. Below this level, Ca^{2+} increases, and both the Mg^{2+} and K^+ decreases downhole are most likely a result of the alteration of basaltic volcanic material, which is observed throughout the sediment at this site (see "Lithostratigraphy," p. 4).

In the upper part of the hole (0 to ~75 mbsf), dissolved strontium concentrations (Sr^{2+}) do not vary significantly (Fig. F16L; Table T14). Below this interval, Sr^{2+} increases continuously, reaching the values of 272.1 mM near the bottom of the hole. This increase below 75 mbsf most likely reflects dissolution of biogenic silica and/or reactions involving alteration of volcanic glass.

Lithium and Silica

Dissolved lithium concentration remains in a narrow range (21–37 mM), similar to that observed in Site 1144 (Fig. F16K; Table T14). In Site 1145, the upper part of the lithium (Li^+) profile exhibits a significant increase in concentrations from 21.5 mM at the top to 37 mM at ~72.4 mbsf (Fig. F16K; Table T14). Below this level, the Li^+ decreases to 27 mM at 127.9 mbsf, then increases again to reach 32.8 mM at the bottom of the hole. The low Li^+ concentrations at the top of the hole are probably a result of an uptake of Li^+ during authigenic calcite precipitation.

Dissolved silica (H_4SiO_4) increases slightly at the top of the hole to 846 mM at 24.9 mbsf and then is high and constant between 24.9 to 72.4 mbsf. Below this interval, H_4SiO_4 concentrations decrease abruptly and then vary within a lower range of values from 220–276 mM (Fig. F16L; Table T14). This shift was also observed at the higher accumulation rate Site 1144 at 388.5 mbsf (see "Inorganic Geochemistry," p. 17, in the "Site 1144" chapter) and is synchronous (~1 Ma) in both sites.

In Sites 1144 and 1145, this shift coincides with the major lithologic change at this site, which is expressed best as an increase in the magnetic susceptibility record (see "Physical Properties," p. 15). This lithologic change is also characterized by a decrease of the biogenic silica

(opal-A) content (see "Biostratigraphy," p. 7), which is likely responsible for the decrease of H_4SiO_4 and Li^+ below 72.4 mbsf.

PHYSICAL PROPERTIES

Sampling

At Site 1145, physical properties were measured on whole-round sections, split-core sections, and discrete samples from the latter. Whole-core logging with the MST included GRA bulk density, MS, NGR, and *P*-wave velocity logging on all cores. Sampling intervals were 5 cm for all cores in the three holes. One thermal conductivity measurement per core was also performed on the whole-round sections. Color spectral reflectance was measured on the archive halves of all split cores at 4-cm intervals. Moisture, density, and *P*-wave velocity were measured on discrete samples from split-core sections at intervals of one measurement per section (1.5 m) (see "Physical Properties," p. 18, in the "Explanatory Notes" chapter). The *P*-wave logger (PWL) data were bad because of instrument problems and/or cracks or voids in the sediment cores. The PWL data are not shown in this report but are available from the ODP JANUS database (see the "Related Leg Data" contents list).

Results

Core physical properties measurements show three major features. The first one is related to the change from APC to XCB coring (136.23 mcd in Hole 1145A, 134.16 mcd in Hole 1145B, and 132.86 mcd in Hole 1145C). The XCB cores are moderately disturbed by partial remolding and incorporation of drilling slurry. The reduced diameter of XCB cores is probably the main component of the slight offset of GRA, MS, and NGR values at those depths (Figs. F17, F18, F19). This effect is not compensated for because there is no time to perform a careful correction on board ship.

The other two primary features in the core-logging data are related to changes in sediment composition. One is the cyclical fluctuations of data from the MST over the entire section (Figs. F17, F18, F19). The other characteristic is an abrupt downhole increase in GRA, MS, and NGR values, accompanied by a decrease in porosity, at 80 mcd (Figs. F17, F18, F19, F20). These increasing downhole trends level out at ~140 mcd. These features are described in the next section.

Multisensor Track Parameters, Porosity, and Grain Density

The GRA, MS, and NGR data show high-amplitude cyclicity over the entire interval recovered (Figs. F17, F18, F19). These cycles are best defined in the NGR data, where the dominant wavelength changes at ~75 mcd from ~10–15 m in the upper interval to ~2–5 m in the lower interval. These fluctuations are interpreted as glacial–interglacial compositional changes. Based on preliminary correlations with oxygen isotope reference curves and chronostratigraphic results (see "Sedimentation and Accumulation Rates," p. 10), the change in cyclicity occurs at ~0.4 Ma and is associated with a fourfold increase in sedimentation rate from the lower to the upper interval.

Below the change in dominant wavelength at ~75 mcd, the average values of GRA, MS, and NGR roughly double (Figs. F17, F18, F19). The

F17. Bulk density measurements from GRA and MAD methods, p. 39.
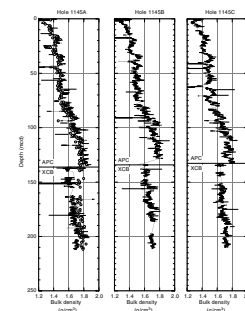
F18. Magnetic susceptibility measurements, p. 40.
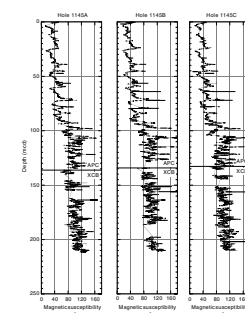
F19. Natural gamma radiation measurements, p. 41.
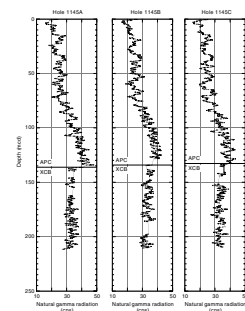
abrupt increase in these values is accompanied by a sudden decrease in porosity from ~70% to ~55% (Fig. F20). Porosity appears to clearly define an interval of excursion from a linear trend connecting the uppermost 75 mcd with the interval below 170 mcd. The porosity decrease alone cannot account for the changes observed in MS and NGR over the interval from 75 to 170 mcd. We therefore infer a significant change in lithology that also affects porosity and, thus, bulk density. Near 75 mcd, a change in grain density to slightly higher (from ~2.65 to ~2.70 g/cm^3) and less variable values is also observed and supports the interpretation of a change in mineralogic composition (Fig. F20). Shore-based analysis of the sediments will reveal the components and sources affecting this change.

At ~133 mcd, GRA bulk density shows a sharp offset caused by the change from APC to XCB coring. This becomes clear when comparing the bulk density data derived from GRA with the more accurate data obtained from the moisture and density (MAD) method, which do not show the offset at that depth (Fig. F17).

Color Spectral Reflectance

The CSR data are presented as records of two parameters from the L*a*b* color system: L*, representing the lightness in percent; and a*/b*, the ratio of the two chromaticity parameters (Fig. F21). L* can be used as a first-order approximation to the relative concentration of carbonate. This correlation is not yet readily apparent because shipboard carbonate measurements were done at a low sampling resolution. There is no major downhole trend in either the carbonate concentrations or L*. Cyclic changes are present throughout the L* record and correlate with those seen in other parameters and interpreted as glacial–interglacial cycles. The a*/b* ratio is a proxy for color change that can be related to a combination of carbonate or organic matter content, clay mineralogy, oxidation, and so forth. A distinct minimum and subsequent inversion is observed at ~88 mcd and can be related to the change in lithology indicated by all other parameters at ~75 mcd.

P-wave Velocity

In the uppermost 58 mcd, *P*-wave velocity sensor PWS1 and PWS2 values are at ~1520 m/s and show little variability (Fig. F22). Below that depth, values sharply increase and fluctuate between ~1550 and ~1680 m/s (Fig. F22). The abrupt change at 58 mcd is the result of an operational error that produced inaccurate transducer displacement measurements. The higher velocities in the lower interval were therefore overestimated.

Thermal Conductivity

Thermal conductivity data from the APC and XCB cores range from 0.85 to 1.15 W/(m·K) (Table T15, also in ASCII format; Fig. F23). The values from XCB cores are compromised by core quality, particularly in the upper XCB interval. The values from APC cores show a relatively linear, downhole increasing trend. A slight increase at ~80 mcd is observed, which corresponds to a downhole gain in bulk density at that depth.

F20. Porosity from MAD measurements grain density, and dry density for Hole 1145A, p. 42.
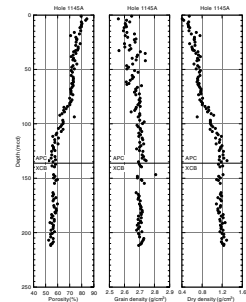
F21. Color reflectance measurements, p. 43.
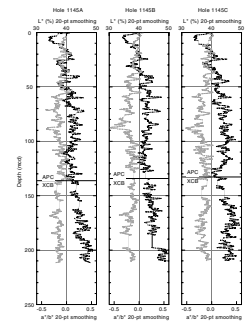
F22. *P*-wave velocity measurements for Hole 1145A, p. 44.
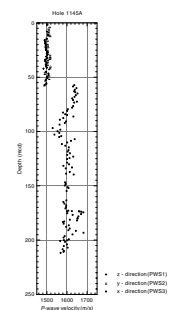
T15. Thermal conductivity measurements, p. 63.

Downhole Temperature Gradient

Three downhole temperature measurements with the APC temperature tool were taken in Hole 1145A at depths of 29.9, 58.4, and 96.4 mbsf, respectively. Also, a bottom-water temperature measurement was taken before coring in Hole 1145B (Fig. **F24**). The objective was to establish the local heat flow. Original temperature records were analyzed using "Tfit" software to establish the equilibrium temperature at depth. The estimated errors in equilibrium temperature vary from 0.2° to 0.4°C, reflecting the amount of frictional head introduced near the sensors during the 10-min measurements. Depth errors are on the order of ±0.5 m. The measurements between 0 and 96.4 mbsf yielded a thermal gradient of 90°C/km (Fig. **F25**).

F23. Thermal conductivity measurements for Hole 1145A, **p. 45.**
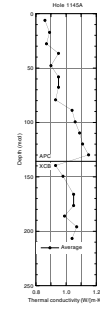
F24. Downhole temperature measurements, **p. 46.**
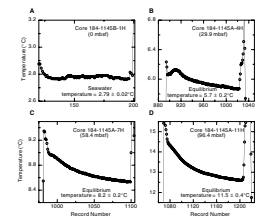
F25. Downhole temperature gradient, **p. 47.**
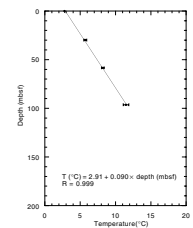
REFERENCES

Blow, W.H., 1969. Late middle Eocene to Recent planktonic foraminiferal biostratigraphy. *In* Brönnimann, P., and Renz, H.H. (Eds.), *Proc. First Int. Conf. Planktonic Microfossils, Geneva, 1967:* Leiden (E.J. Brill), 1:199–422.

Broecker, W.S., and Peng, T.-H., 1982. *Tracers in the Sea:* Palisades, NY (Lamont-Doherty Geol. Observ.).

Carter, R.M., McCave, I.N., Richter, C., Carter, L., et al., 1999. *Proc. ODP, Init. Repts.,* 181 [CD-ROM]. Available from: Ocean Drilling Program, Texas A&M University, College Station, TX 77845-9547, U.S.A.

Katz, B.J., 1983. Limitations of "Rock-Eval" pyrolysis for typing organic matter. *Org. Geochem.,* 4:195–199.

Le, J., and Shackleton, N.J., 1992. Carbonate dissolution fluctuations in the western equatorial Pacific during the late Quaternary. *Paleoceanography,* 7:21–42.

Li, B., 1997. Paleoceanography of the Nansha Area, southern South China Sea since the last 700,000 years [Ph.D. dissert.]. Nanjing Inst. Geol. Paleontol., Academica Sinica, Nanjing, China. (in Chinese, with English abstract)

Redfield, A.C., Ketchum, B.H., and Richards, F.A., 1982. The influence of organisms on the composition of seawater. *In* Hill, M.N. (Ed.), *The Sea* (Vol. 2): New York (Wiley), 26–49.

Riebesell, U., Wolf-Gladrow, D.A., and Smetacek, V., 1993. Carbon dioxide limitation of marine phytoplankton growth rates. *Nature,* 361:249–251.

Romankevich, E.A., 1984. *Geochemistry of Organic Matter in the Ocean:* New York (Springer-Verlag).

Sarnthein, M., Pflaumann, U., Wang, P.X., and Wong, H.K. (Eds.), 1994. Preliminary Report on Sonne-95 Cruise "Monitor Monsoon" to the South China Sea. *Rep. Geol.-Palaontol. Inst. Univ. Kiel.,* 68.

Schönfeld, J., 1996. The "*Stilostomella* Extinction": structure and dynamics of the last turnover in deep-sea benthic foraminiferal assemblages. *In* Mogurlevsky, A., and Whatly, R. (Eds.), *Microfossils and Oceanic Environments:* Aberystwyth (Univ. Wales, Aberystwyth Press), 27–37.

Suess, E., and Müller, P.J., 1980. Productivity, sedimentation rate and sedimentary organic matter in the oceans, II. Elemental fractionation. *Coll. Int. CNRS,* 293:17–26.

Thompson, P.R., Bé, A.W.H., Duplessy, J.-C., and Shackleton, N.J., 1979. Disappearance of pink-pigmented *Globigerinoides ruber* at 120,000 yr BP in the Indian and Pacific oceans. *Nature,* 280:554–558.

Figure F1. Smoothed (11-point running average)/correlated MS data and the splice for the three holes at Site 1145 (spliced MS data in this figure are also available in **ASCII format**). The order of the four arrays (the splice and Holes 1145A through 1145C) increases outward from the origin. The hole arrays are offset from each other—and from the splice—by a constant (10.0 × 10⁻⁵ SI units) so that only the splice is plotted relative to the absolute MS value. Lines identify the splice tie points. (Continued on next page.)
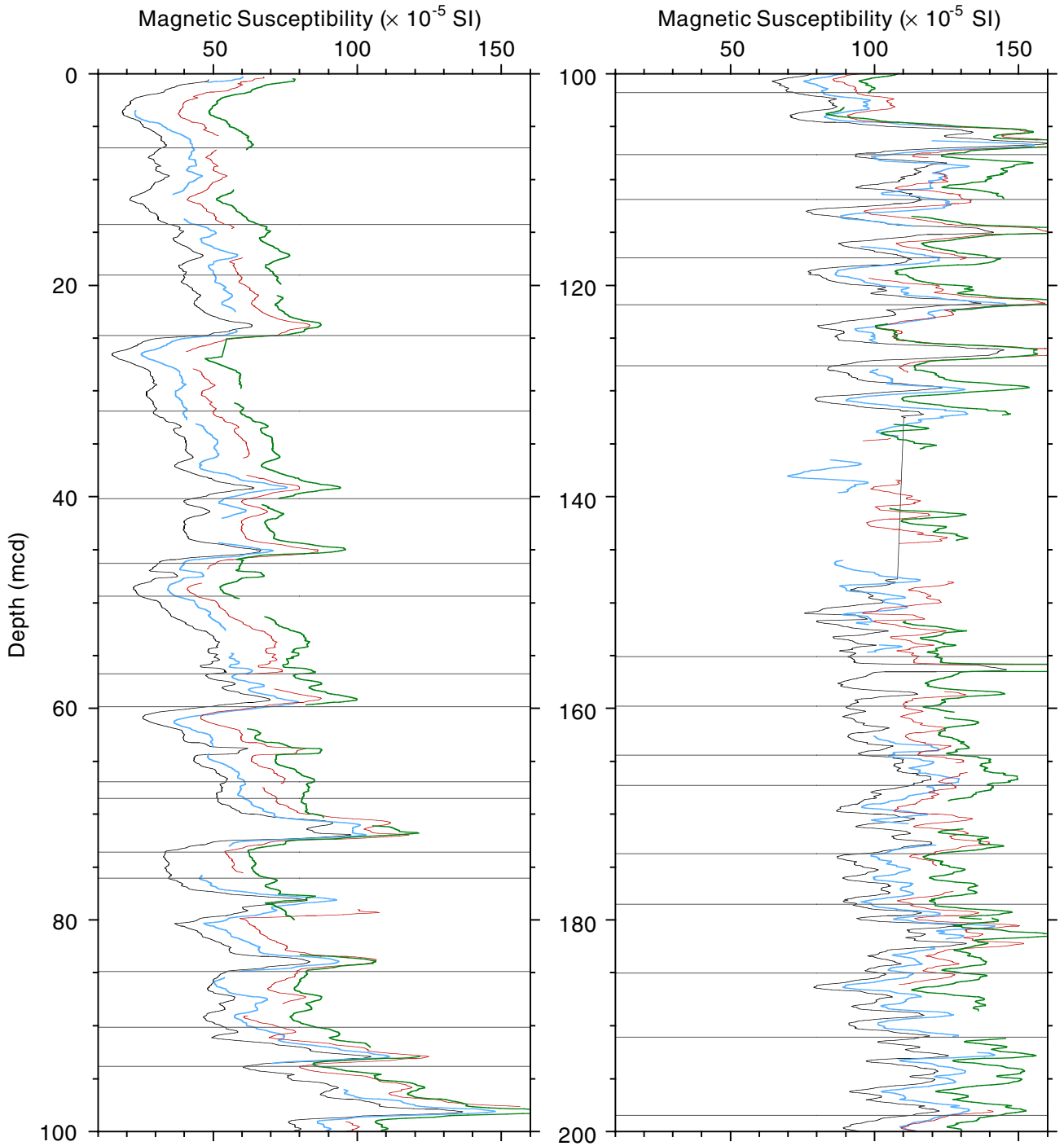
Figure F1 (continued).
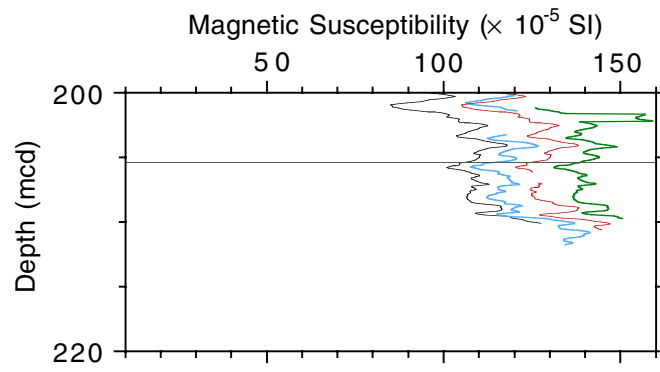
Figure F2. Smoothed (11-point running average)/correlated NGR data and the splice for the three holes at Site 1145 (spliced NGR data in this figure are also available in **ASCII format**). The order of the four arrays (the splice and Holes 1145A through 1145C) increases outward from the origin. The hole arrays are offset from each other—and from the splice—by a constant (9 cps) so that only the splice is plotted relative to the absolute NGR value. Lines identify the splice tie points. (Continued on next page.)
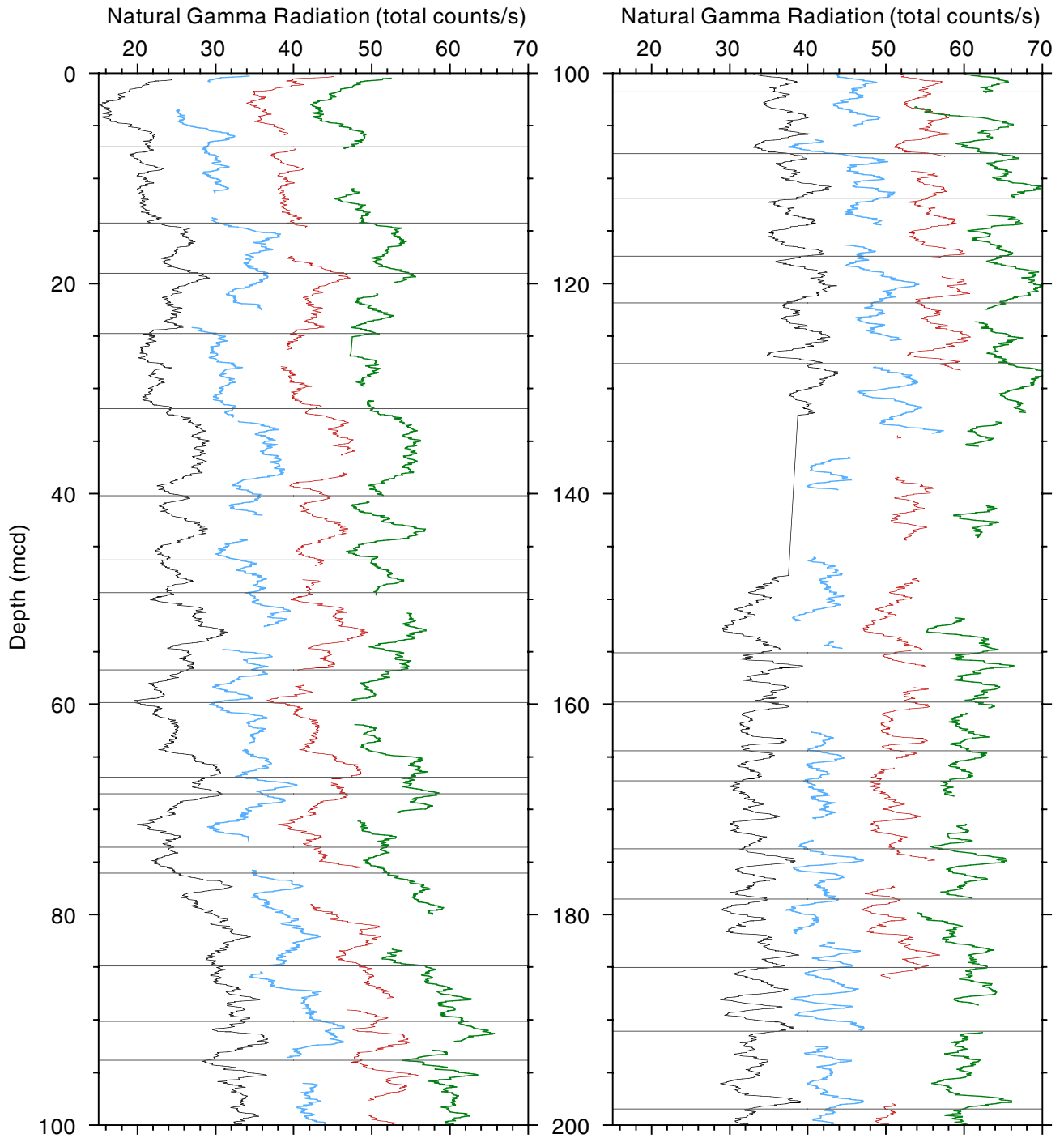
Figure F2 (continued).
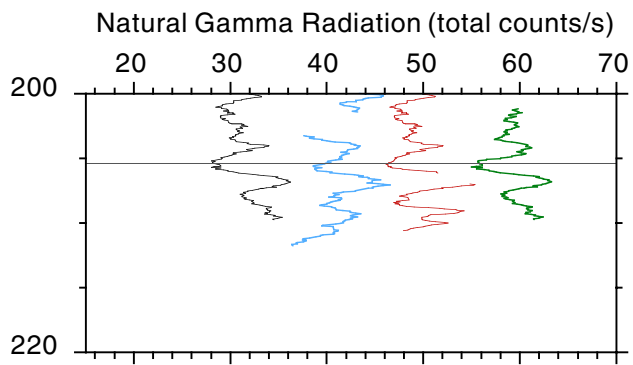
Figure F3. Smoothed (11-point running average)/correlated gamma-ray attenuation (GRA) data and the splice for the three holes at Site 1145 (spliced GRA data in this figure are also available in **ASCII format**). The order of the four arrays (the splice and Holes 1145A through 1145C) increases outward from the origin. The hole arrays are offset from each other—and from the splice—by a constant (0.15 g/cm³) so that only the splice is plotted relative to the absolute GRA value. Values ≤1.03 and ≥2.4 (g/cm³) have been culled. Lines identify the splice tie points. (Continued on next page.)
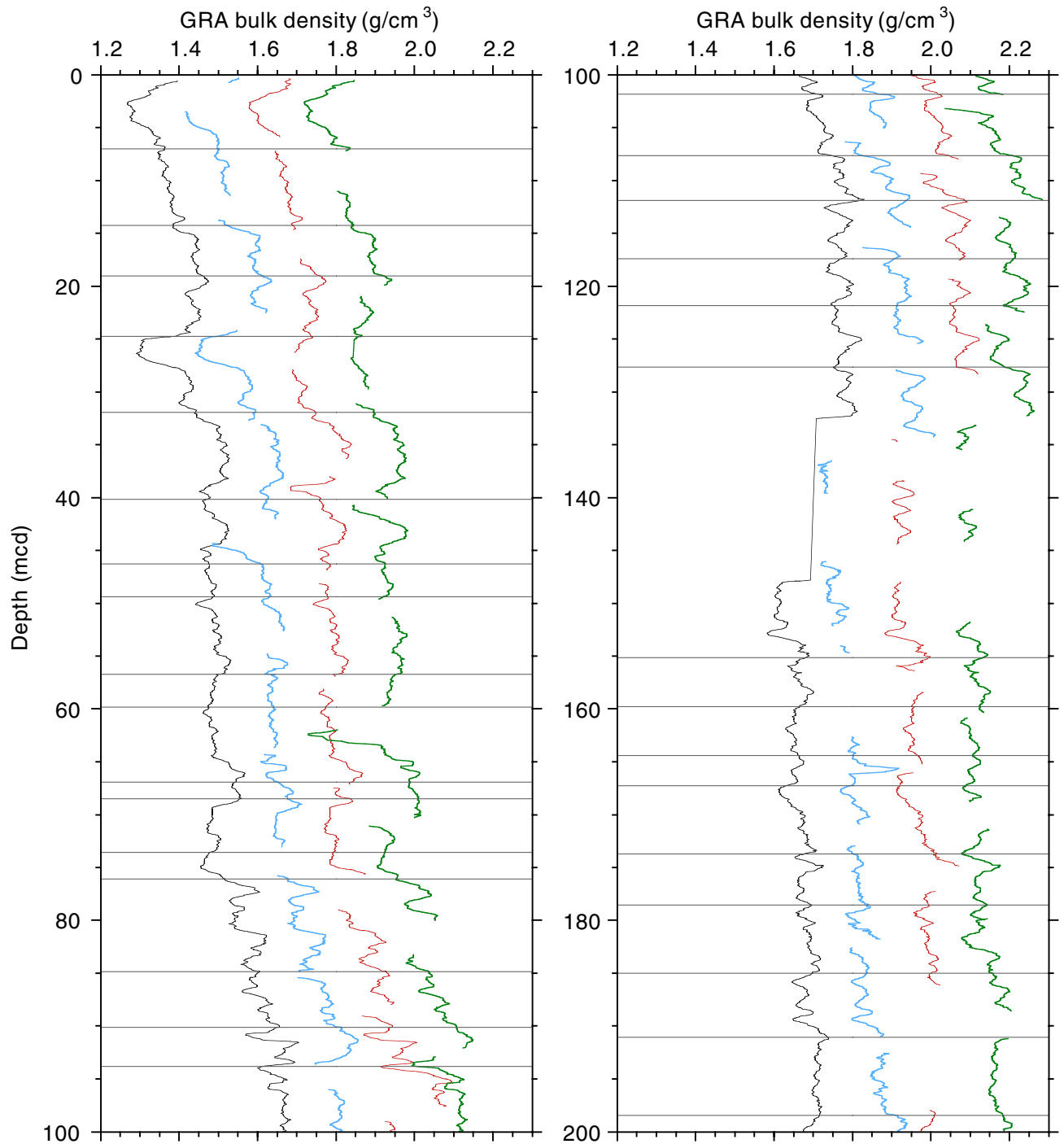
Figure F3 (continued).
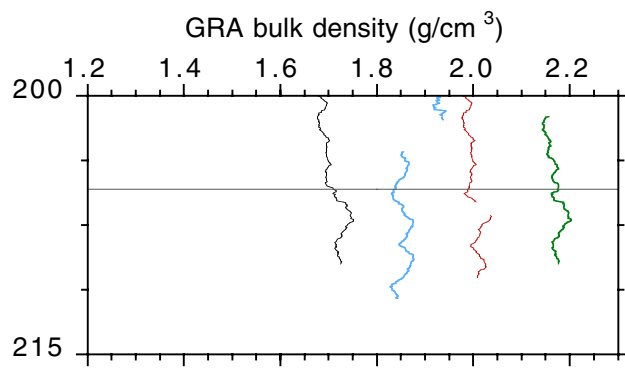
Figure F4. Smoothed (11-point running average)/correlated L* ("lightness") values from the CSR data and the splice for the three holes at Site 1145 (spliced CSR data in this figure are also available in **ASCII format**). The order of the four arrays (the splice and Holes 1145A through 1145C) increases outward from the origin. The hole arrays are offset from each other—and from the splice—by a constant (8%) so that only the splice is plotted relative to the absolute L* value. Values ≤1% have been culled. Lines identify the splice tie points. (Continued on next page.)
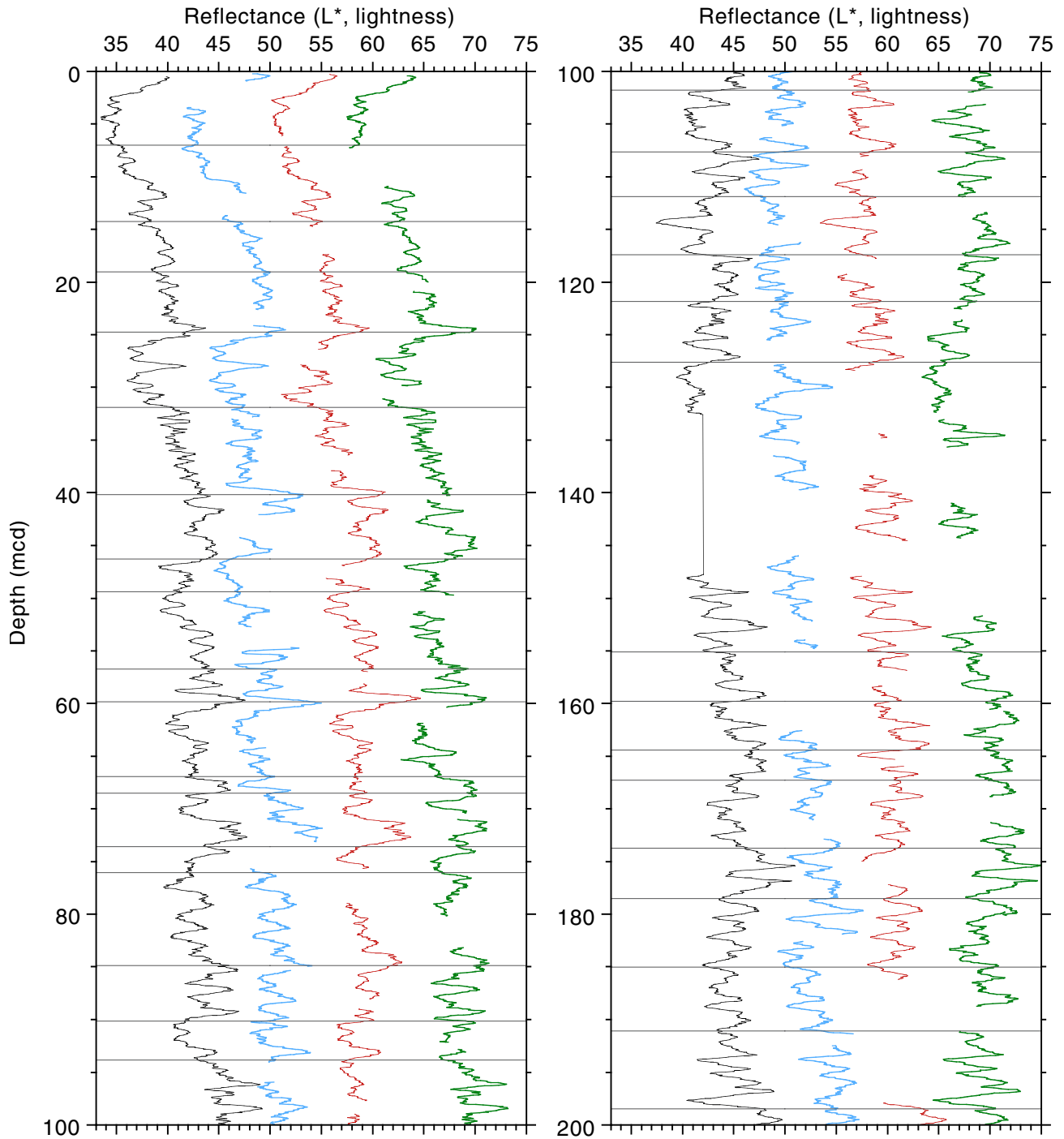
Figure F4 (continued).
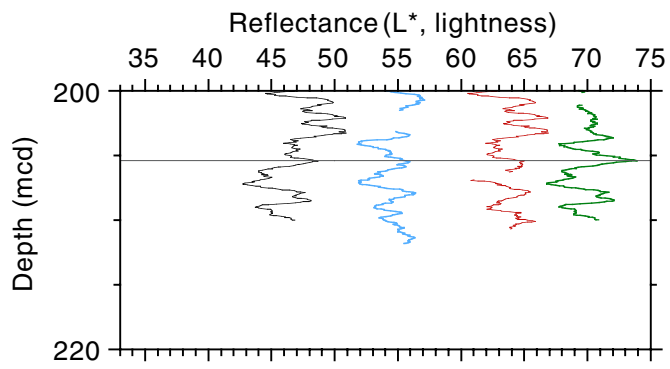
Figure F5. Summary of the recovered section at Site 1145, showing the degree of recovery, lithology, lightness intensity (L* parameter), and the a* parameter. High positive values of a* correspond to high red intensity, whereas high negative values correspond to high green intensity. Proposed correlation with interglacial isotopic stages is indicated by numbers and stars.
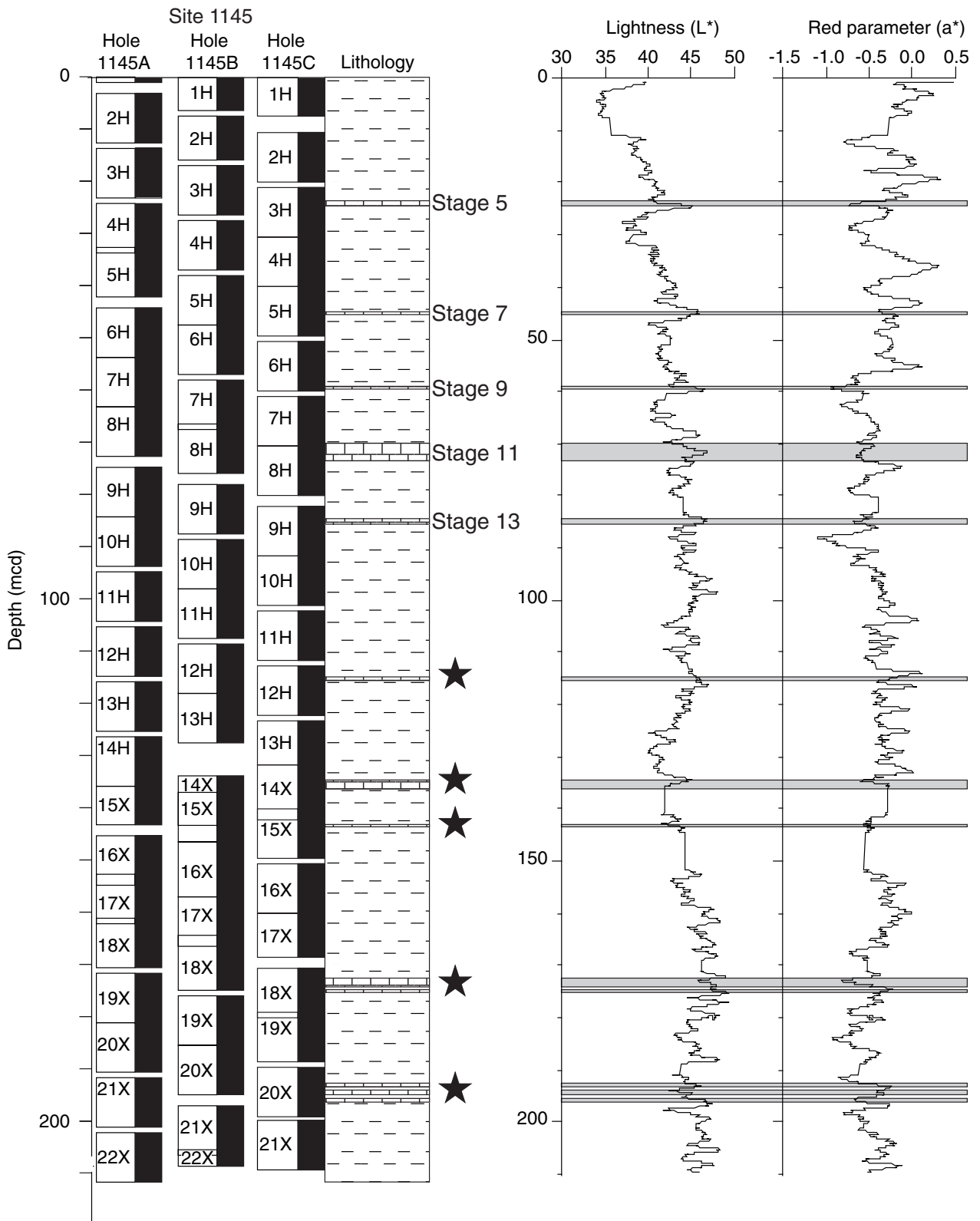
Figure F6. Close-up view of a fecal pellet accumulation replaced by pyrite in interval 184-1145A-15X-1, 1.0–5.5 cm (136.25 mcd).
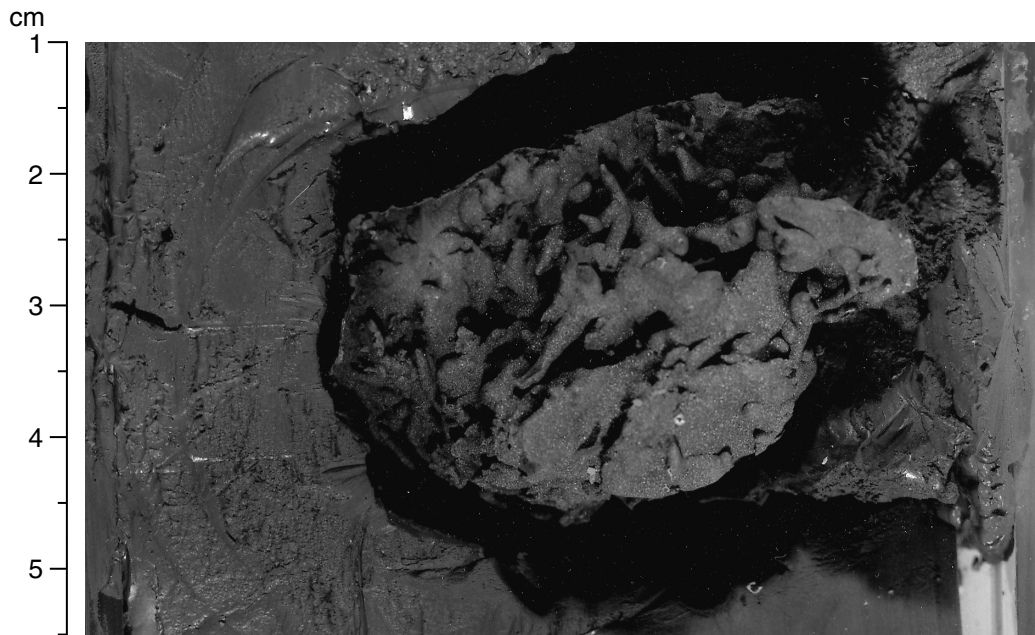
Figure F7. Close-up view of wood at interval 184-1145A-13H-4, 2–10 cm (120.6 mcd).
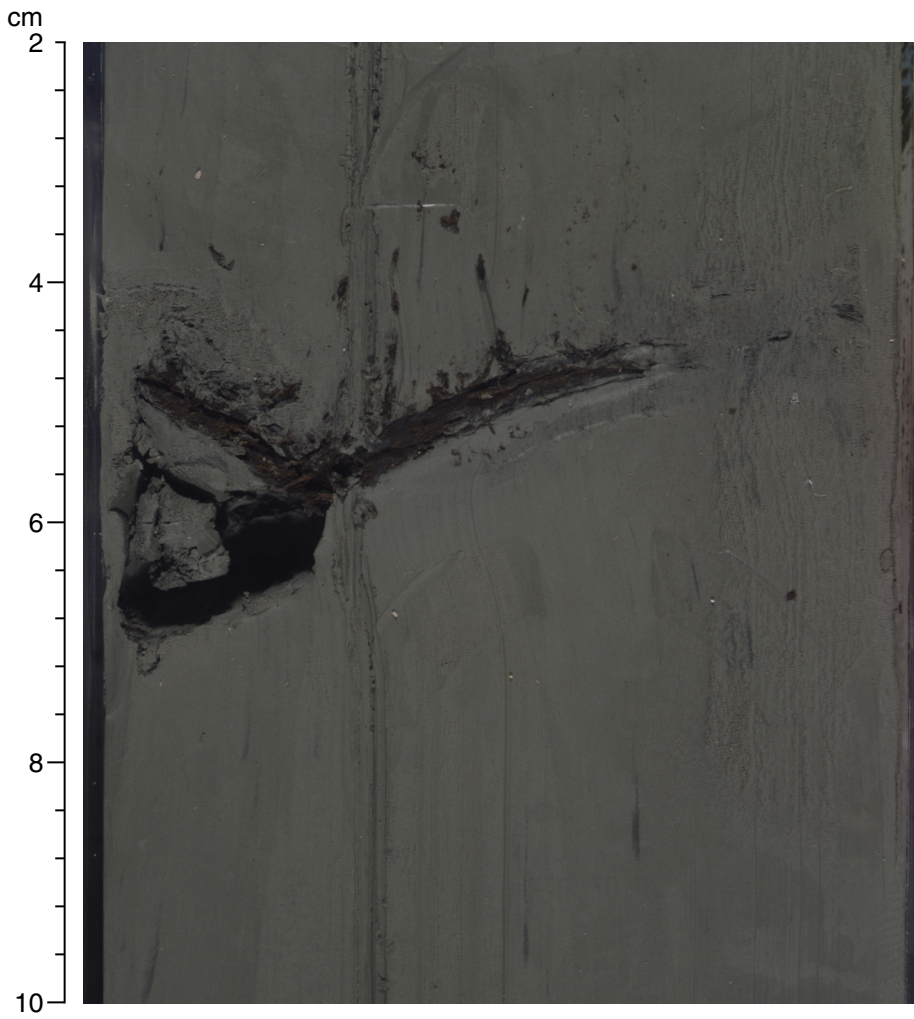
Figure F8. Close-up view of a volcanic ash layer dispersed in burrows (interval 184-1145C-6H-4, 83–95 cm; 56.41–56.46 mcd).
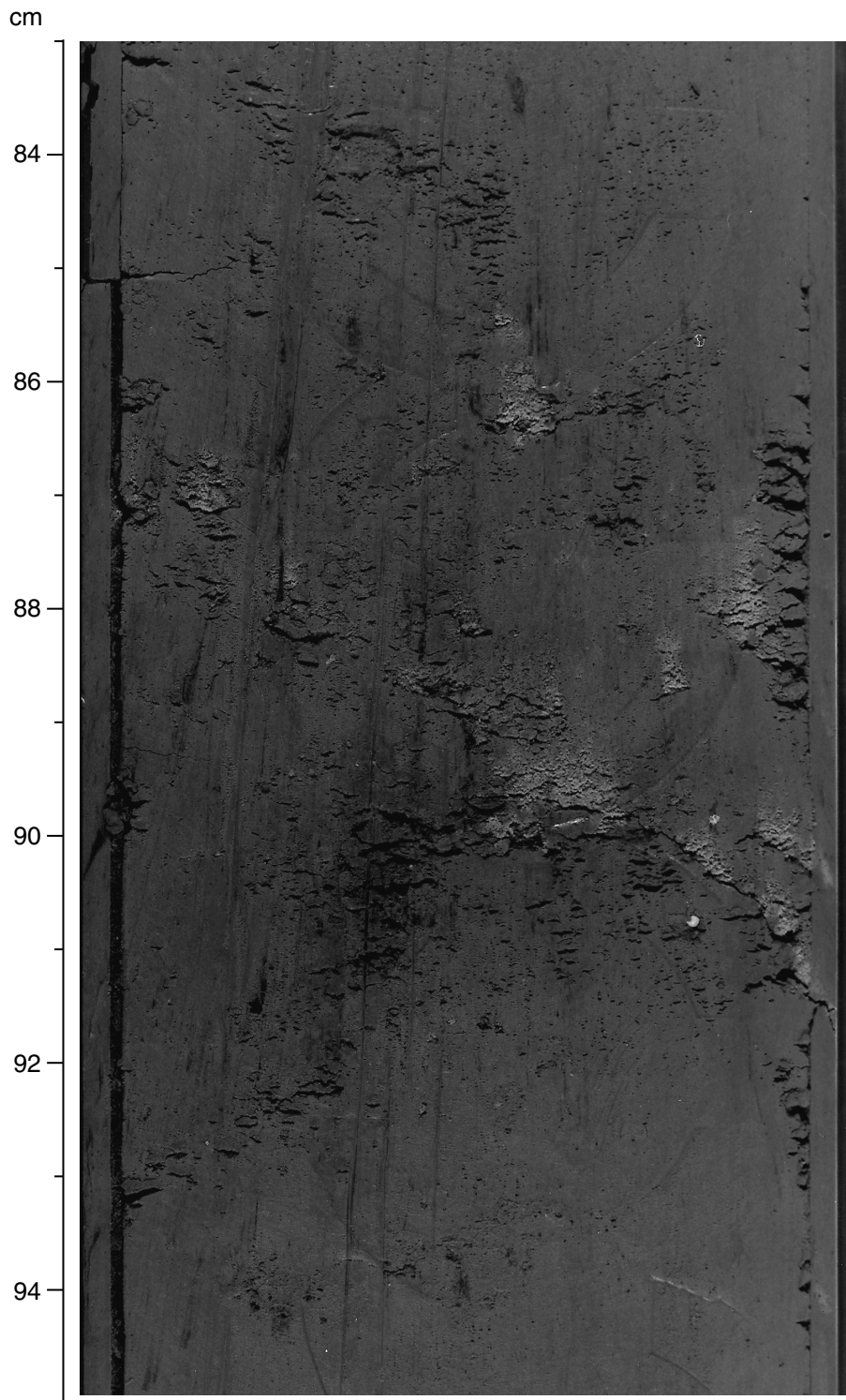
Figure F9. Peak areas of the major mineral components determined by X-ray diffraction for sediment recovered in Hole 1145A. The peak areas only reflect variations in the relative abundance of each mineral downcore; comparisons of concentration between mineral phases are not possible.
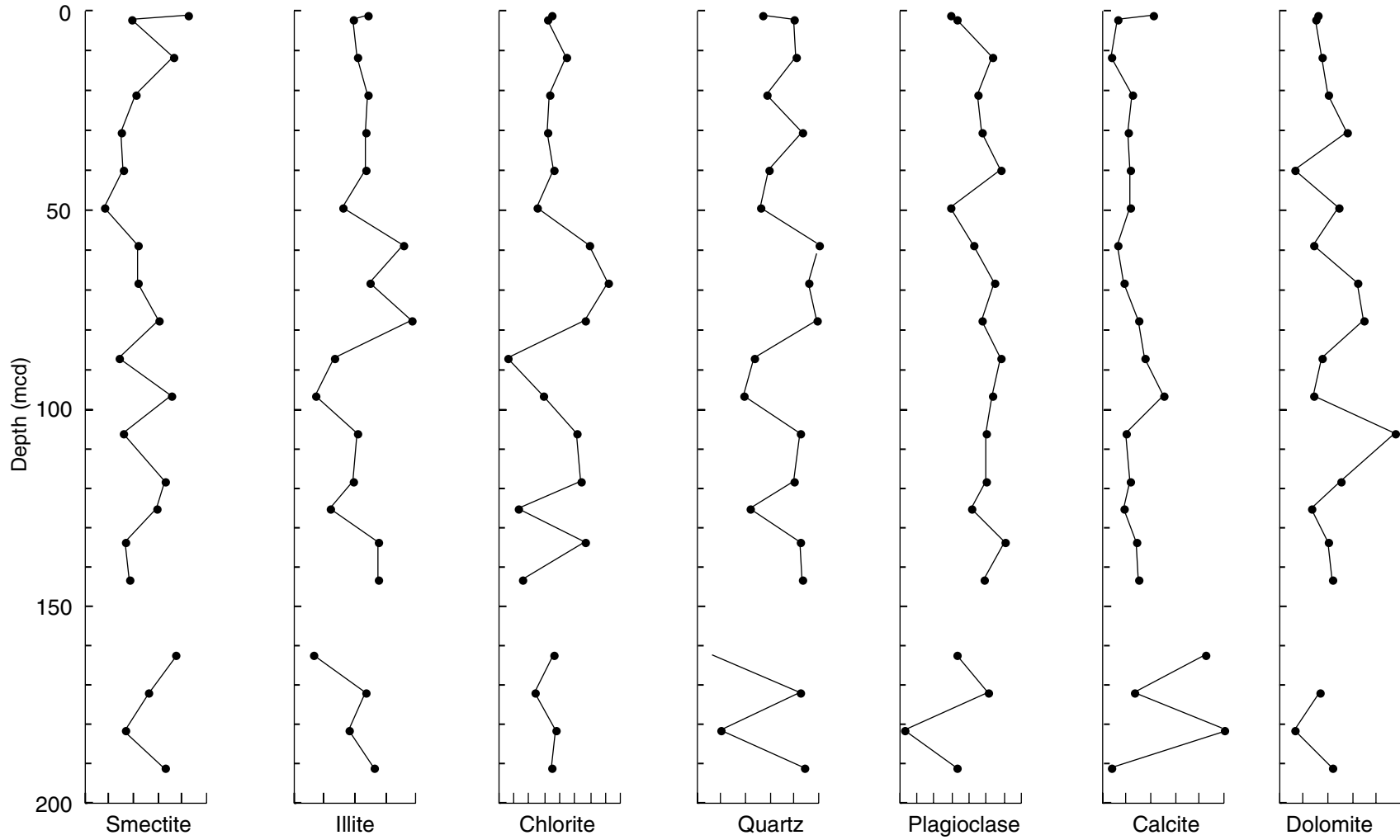
Figure F10. Hole 1145A age-depth plot. All biostratigraphic events are listed in Table T7, p. 55. The average sedimentation rate is calculated based on three control points (control points are marked by * in Table T7, p. 55). Dashed lines = control points selected to define intervals of linear sedimentation rates.
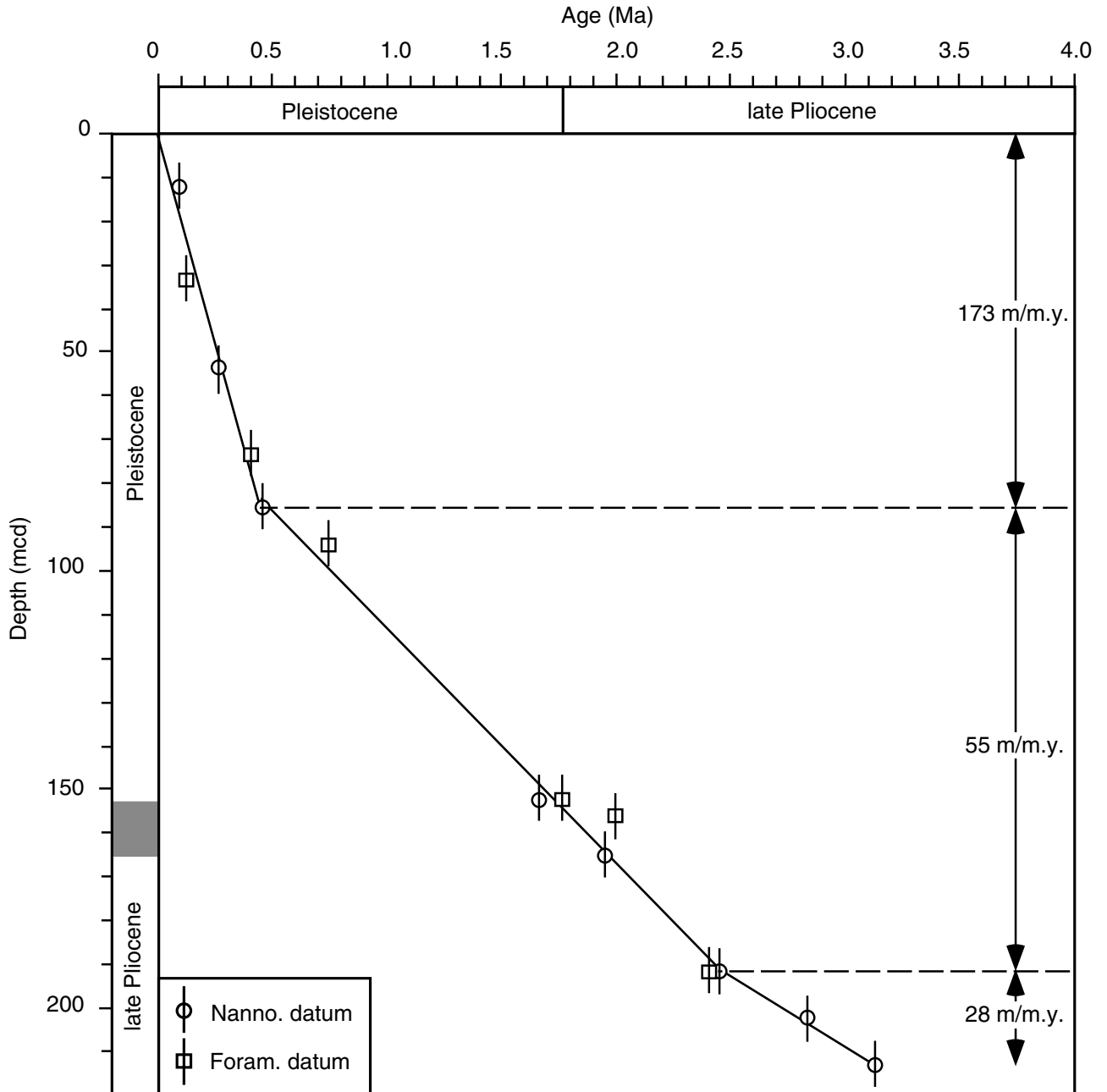
Figure F11. Downhole changes at Hole 1145A in (**A**) planktonic foraminiferal fragmentation, (**B**) the ratio between pteropods (PT) and planktonic foraminifers (PF), and (**C**) the percent abundance of siliceous microfossils (including radiolarians, diatoms, and their debris).
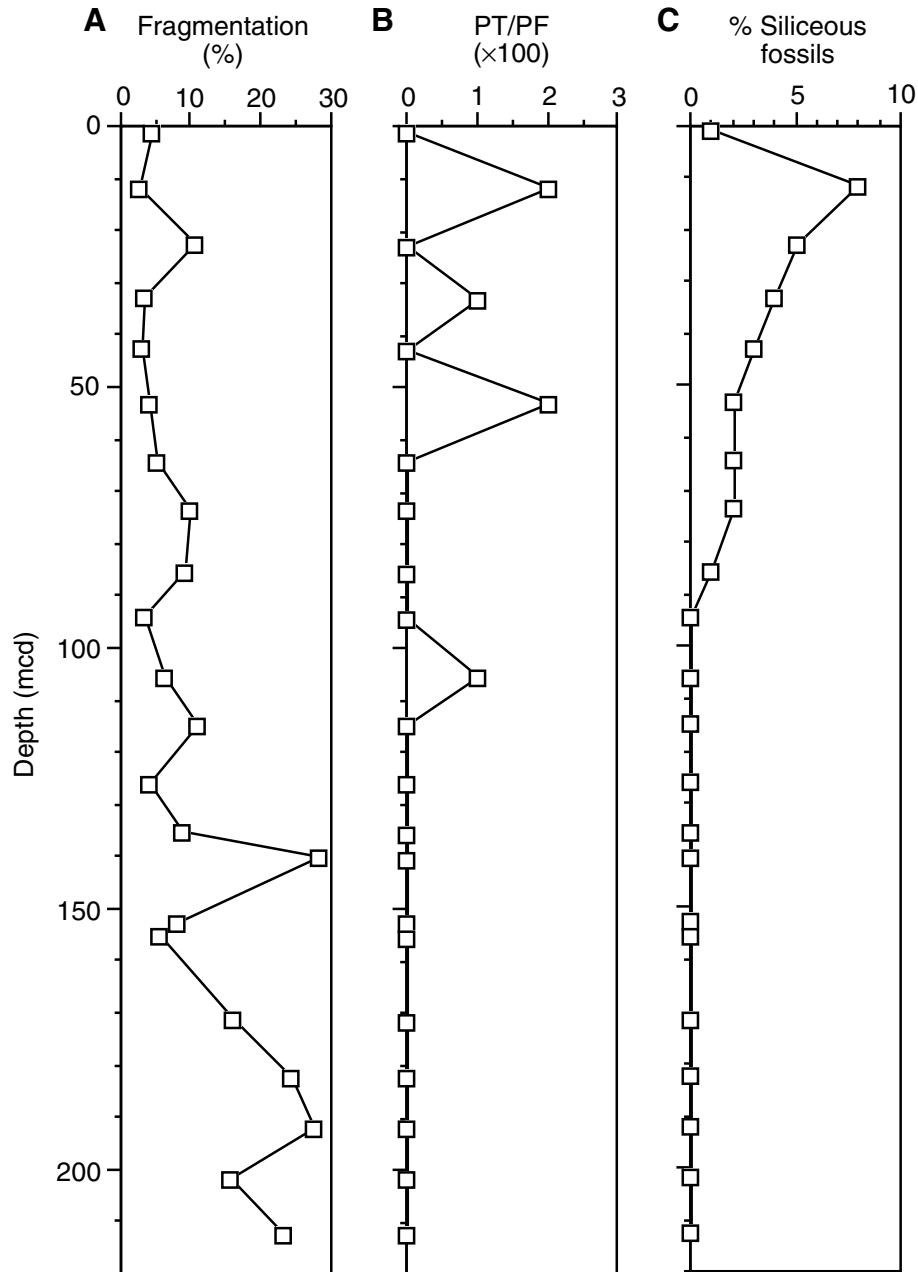
Figure F12. Declination and inclination for Hole 1145A, 0–210 mcd, obtained from long-core measurements (Cores 184-1145A-1H and 2H are not oriented). Below 136 mcd, declination and inclinations are very scattered as a result of XCB cores. Open squares = the inclination results from discrete samples. Black = normal polarity, white = reversed polarity.

Hole 1145A
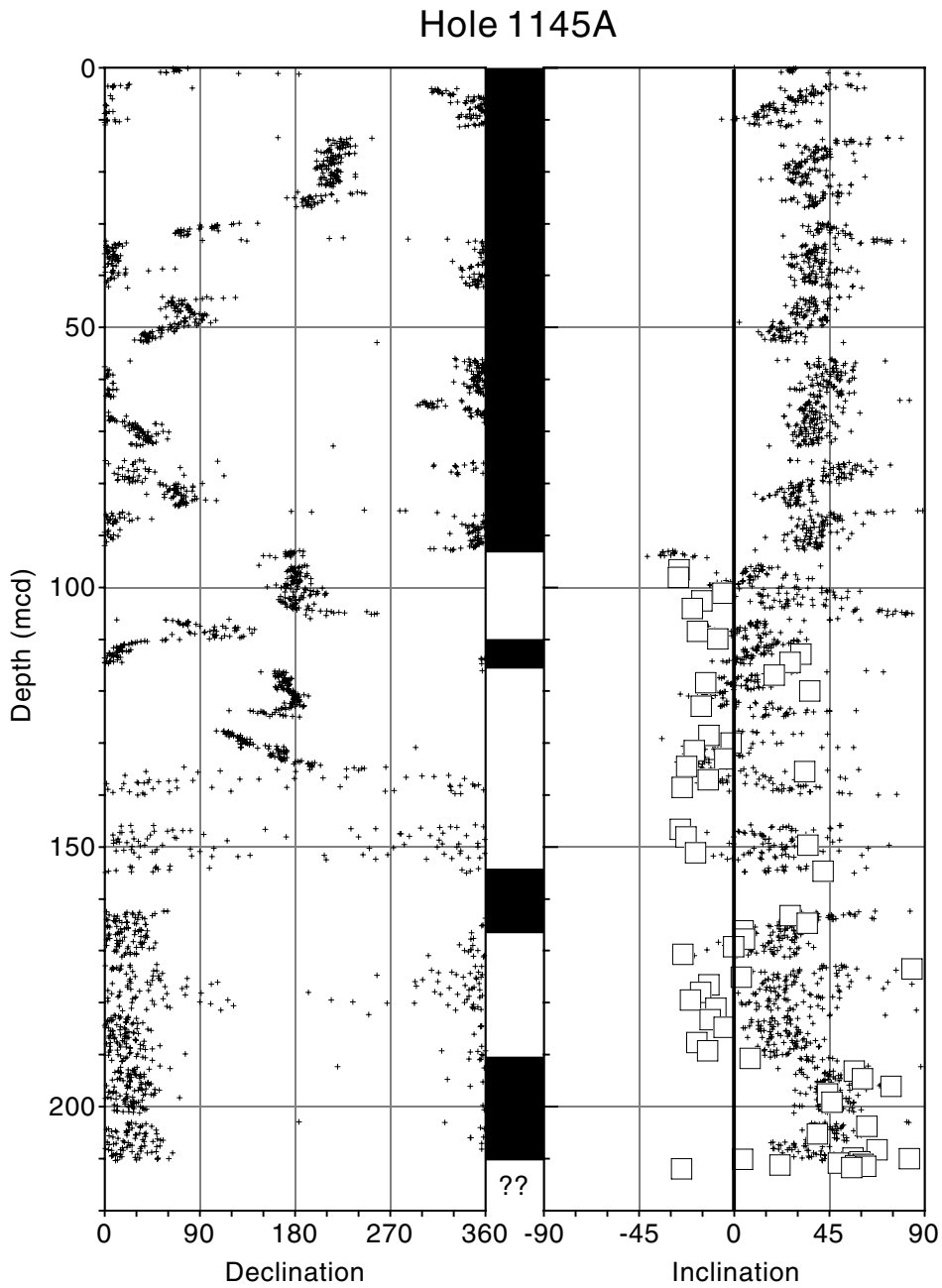
Figure F13. Representative AF demagnetization diagrams from discrete samples, showing (**A**) a sample with normal magnetization and (**B**) a sample with reverse magnetization isolated after removal of the overprint.

A Sample 184-1145A-12H-5, 88 cm
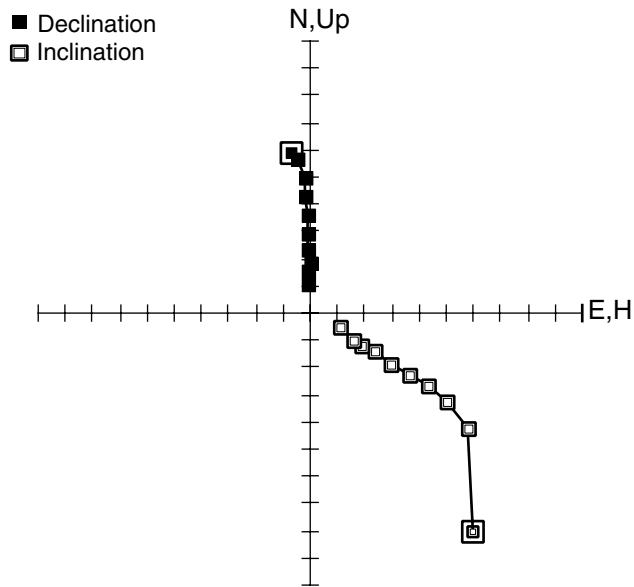
B Sample 184-1145A-13H-5, 88 cm
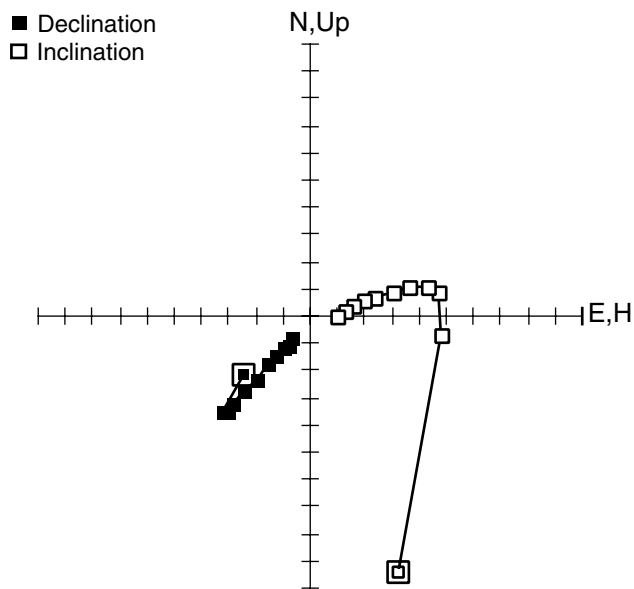
Figure F14. (**A**) Age-depth model, (**B**) linear sedimentation rates (LSR) and mass accumulation rates (MAR) vs. depth, and (**C**) LSR and MAR vs. age for Site 1145. Construction of model rates, LSR, and MAR is explained in **"Sedimentation and Accumulation Rates,"** p. 13, in the "Explanatory Notes" chapter. In (A), diamonds = calcareous nannofossils, circles = foraminifers, squares = paleomagnetic reversals; in (B) and (C), solid lines = total sediment LSR, dashed lines = carbonate LSR, stippled columns = total sediment MAR, solid columns = carbonate MAR. B/M = Brunhes/Matuyama.
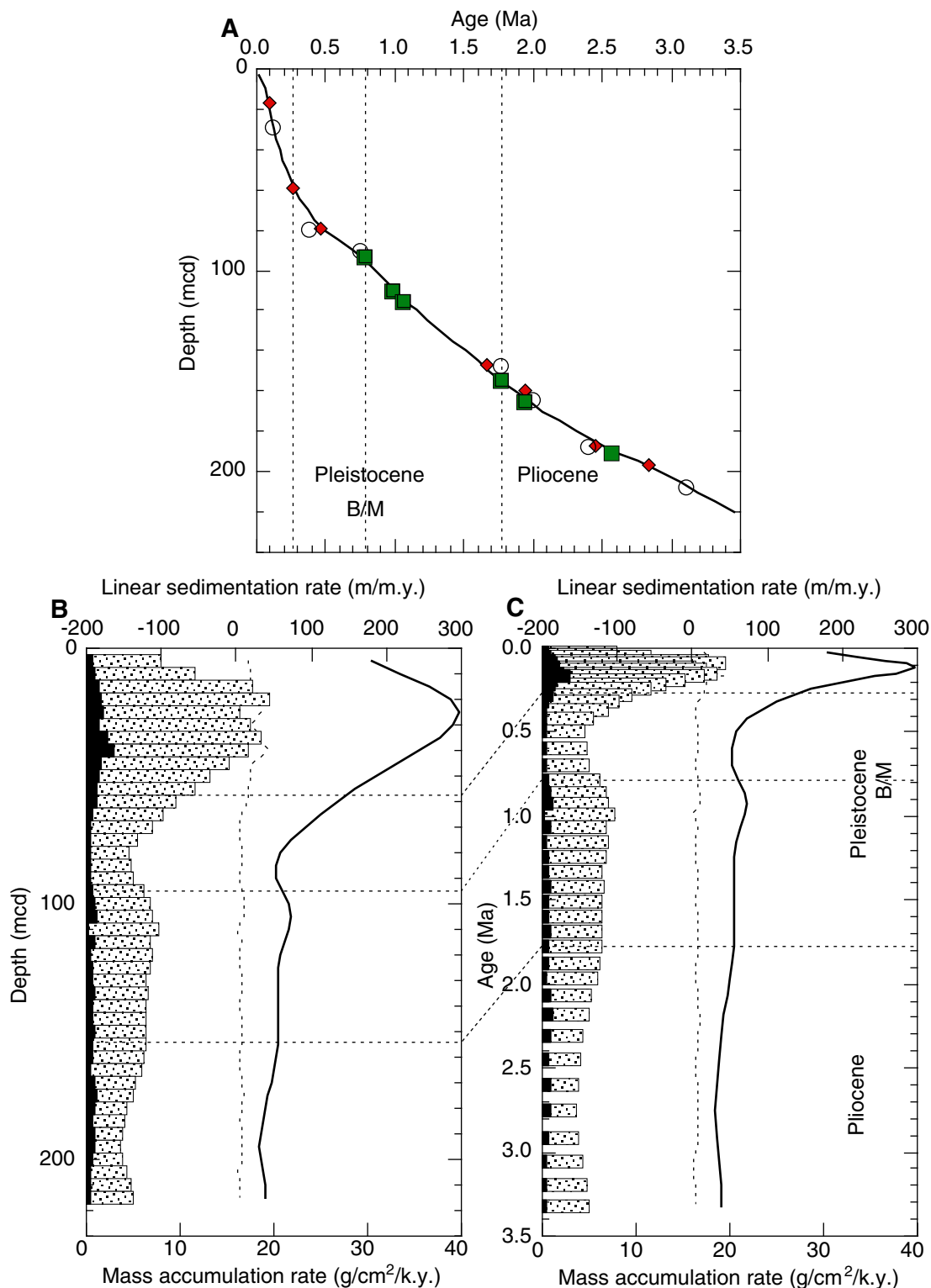
Figure F15. (**A**) Carbonate (wt%), (**B**) total organic carbon (TOC, wt%), and (**C**) organic C/N ratio vs. depth in Hole 1145A.
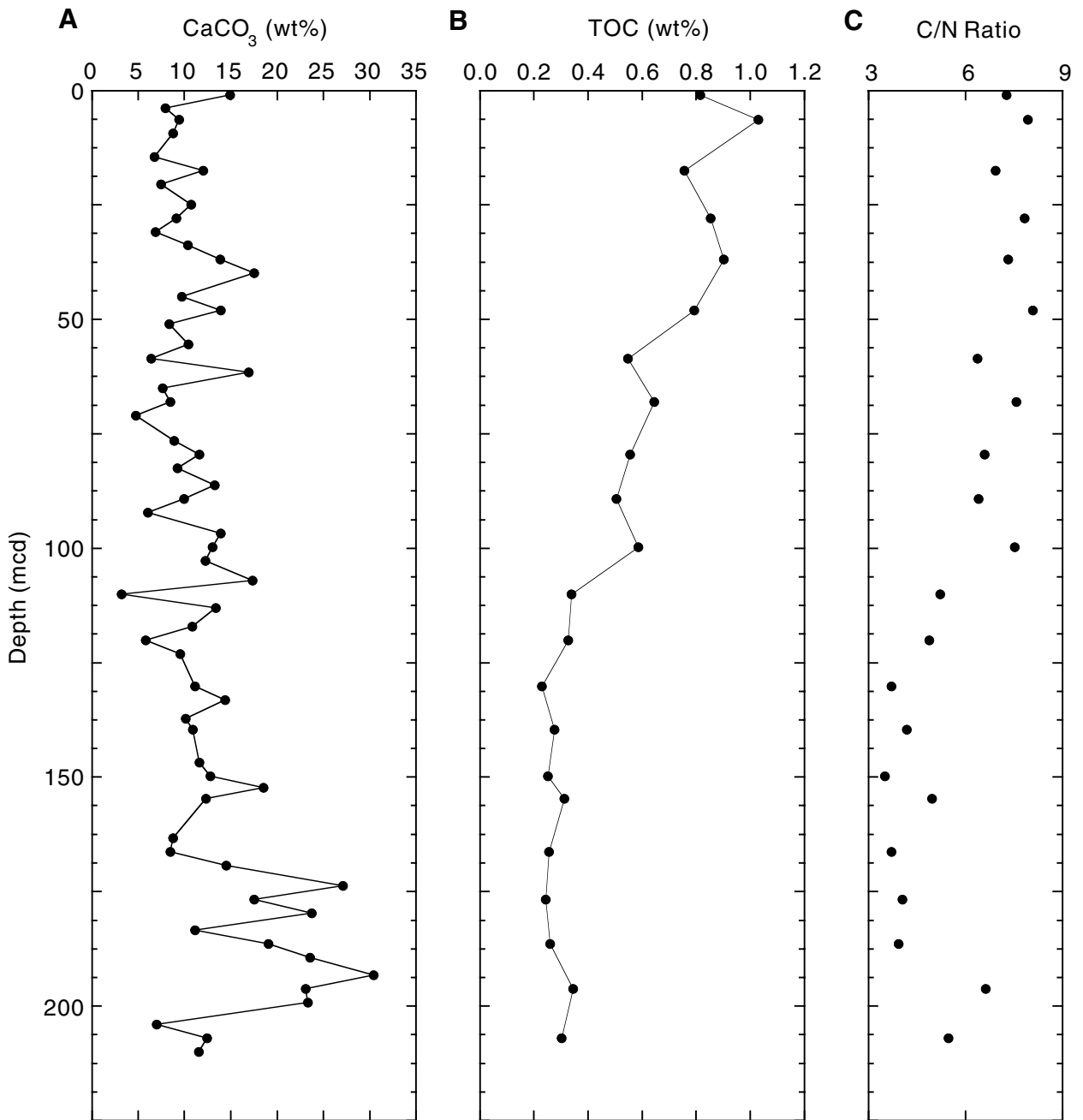
Figure F16. Vertical profiles of interstitial water measurements at Site 1145 (concentrations in Hole 1145A). **A.** Chloride. **B.** Salinity. **C.** Sulfate. **D.** Ammonium. **E.** Phosphate. **F.** Alkalinity. **G.** Magnesium. **H.** Potassium. **I.** Calcium. **J.** Strontium. **K.** Lithium. **L.** Silica.
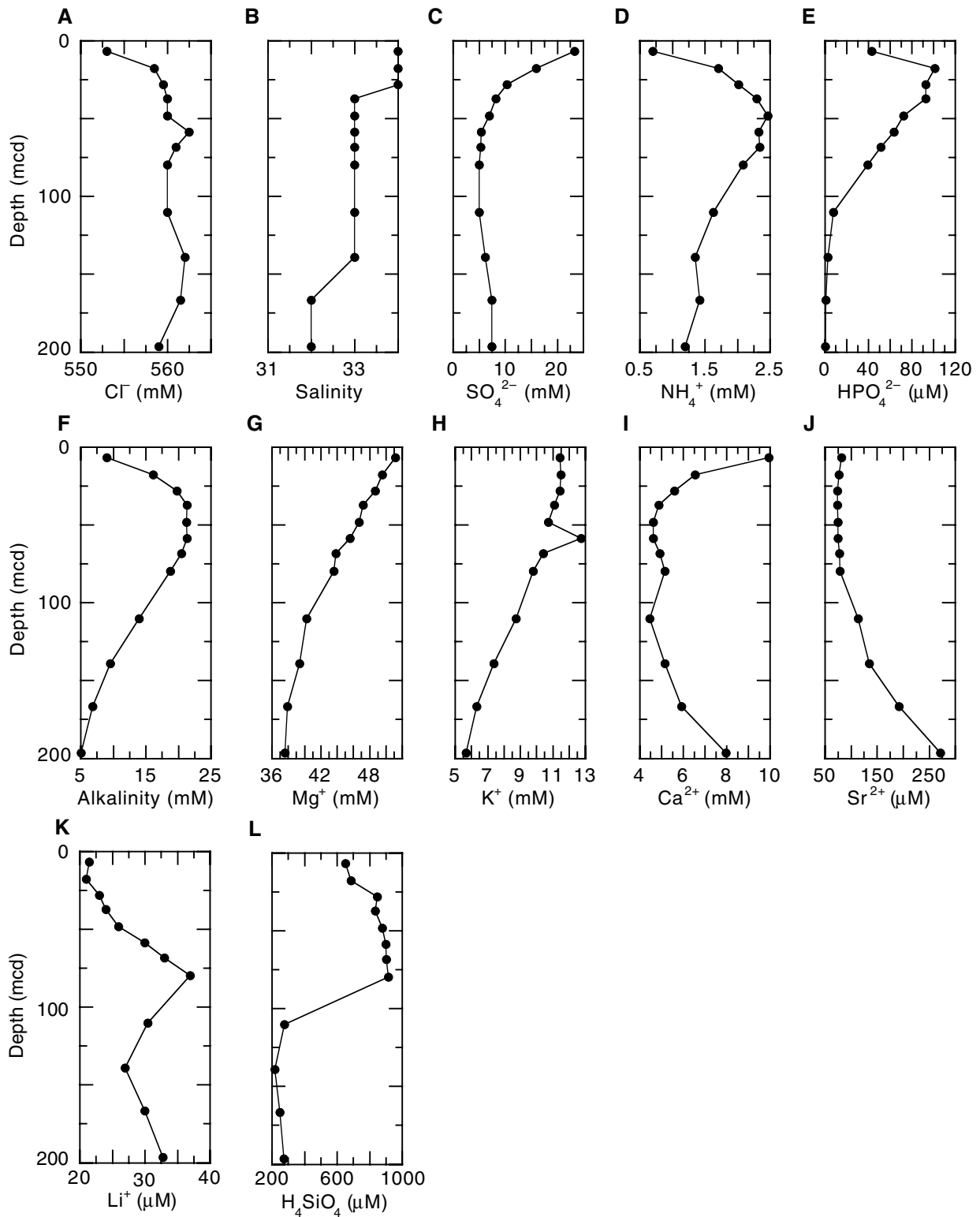
Figure F17. Bulk density measurements from GRA (line) and MAD methods (open circles) for Holes 1145A, 1145B, and 1145C. APC = advanced hydraulic piston corer, XCB = extended core barrel.
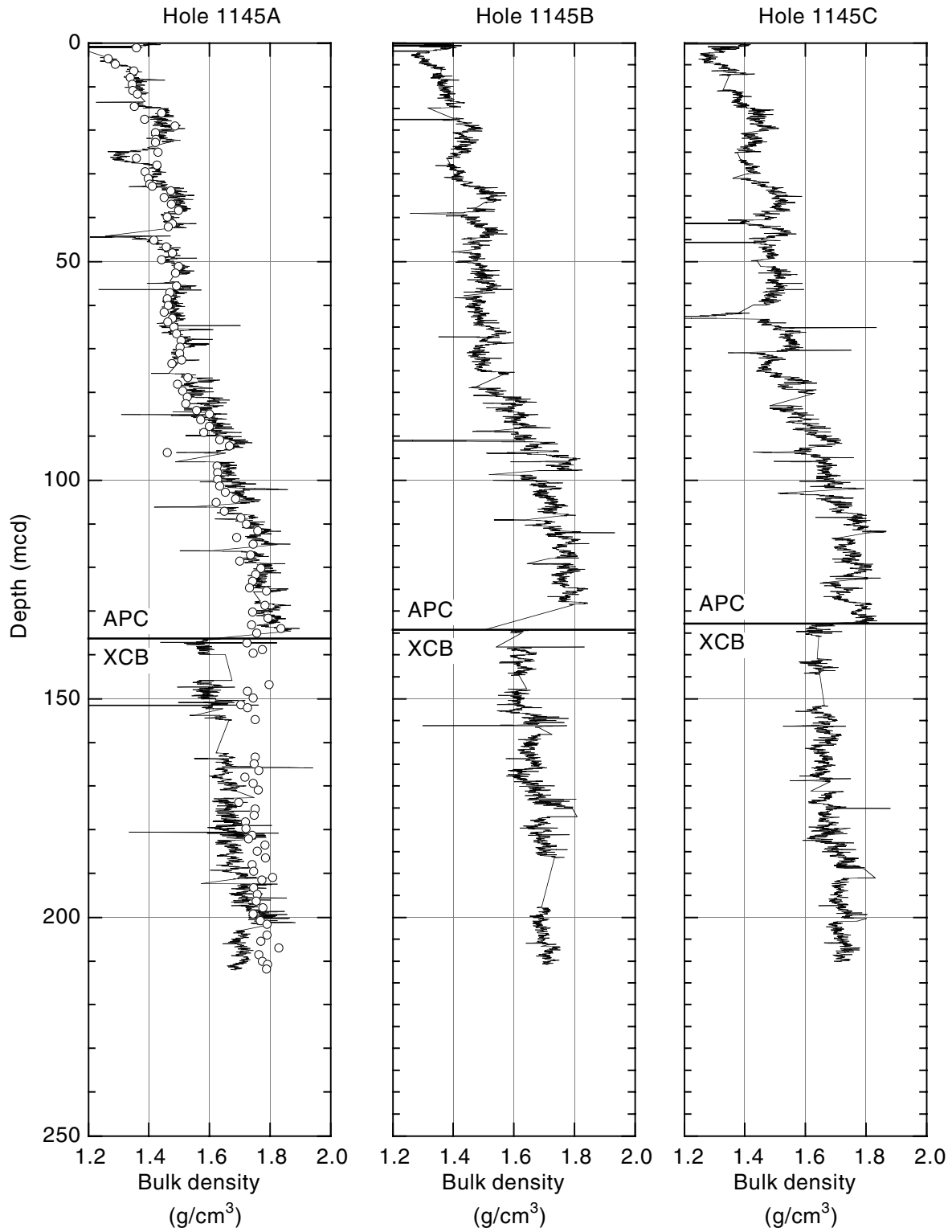
Figure F18. Magnetic susceptibility measurements plotted for Holes 1145A, 1145B, and 1145C. APC = advanced hydraulic piston corer, XCB = extended core barrel.
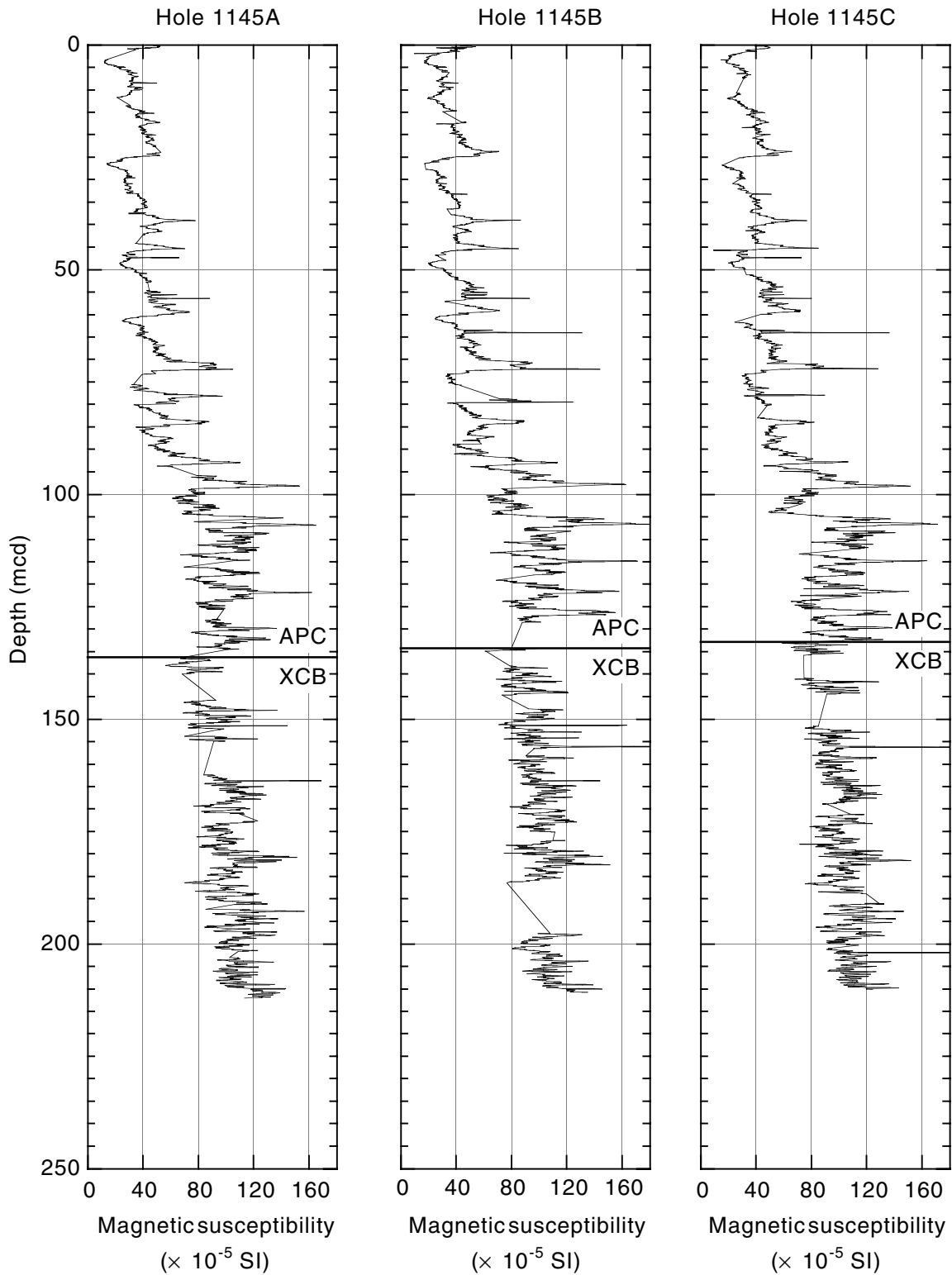
Figure F19. Natural gamma radiation measurements plotted for Holes 1145A, 1145B, and 1145C, smoothed with a 20-point moving average. APC = advanced hydraulic piston corer, XCB = extended core barrel.
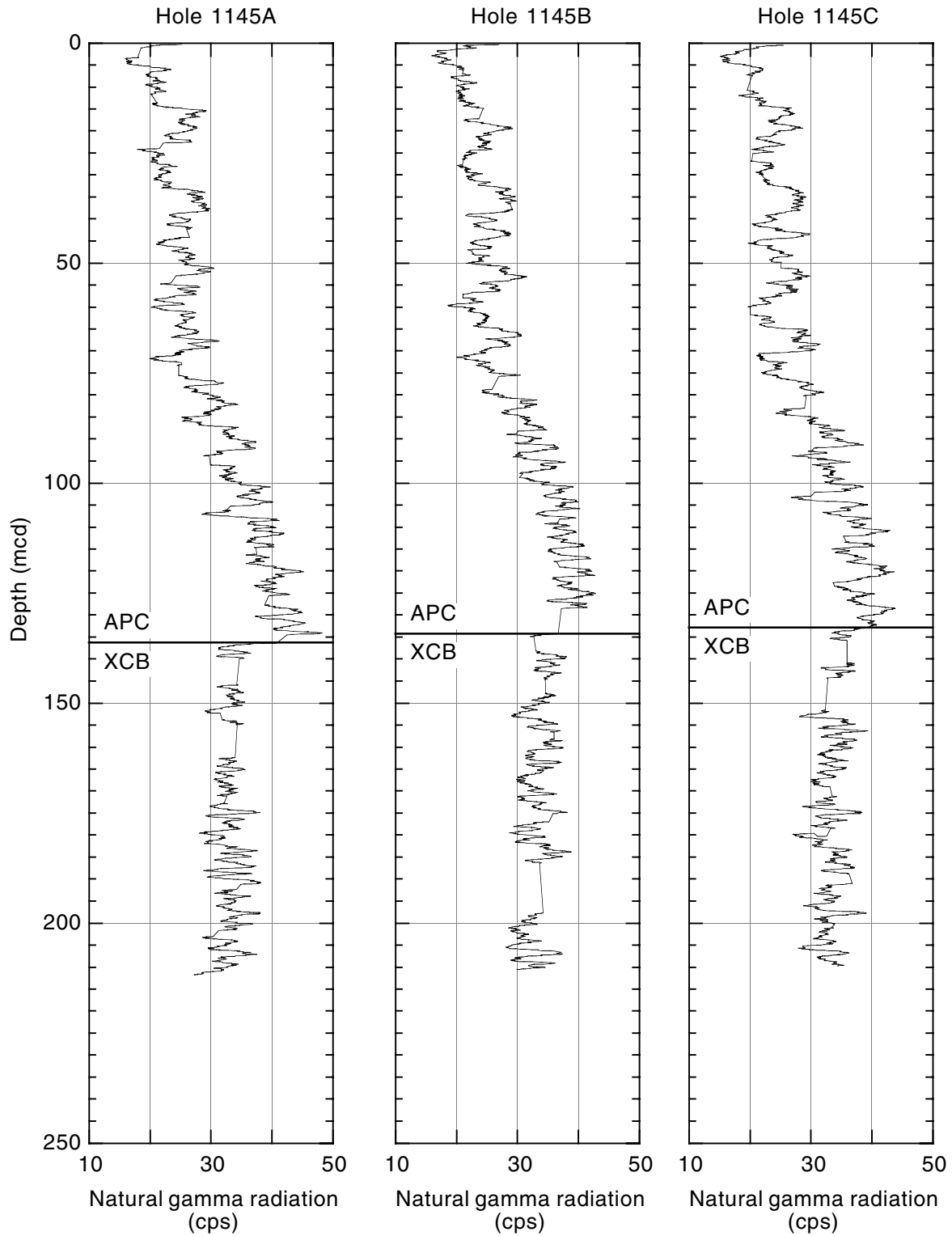
Figure F20. Porosity from MAD measurements, grain density, and dry density plotted for Hole 1145A. APC = advanced hydraulic piston corer, XCB = extended core barrel.
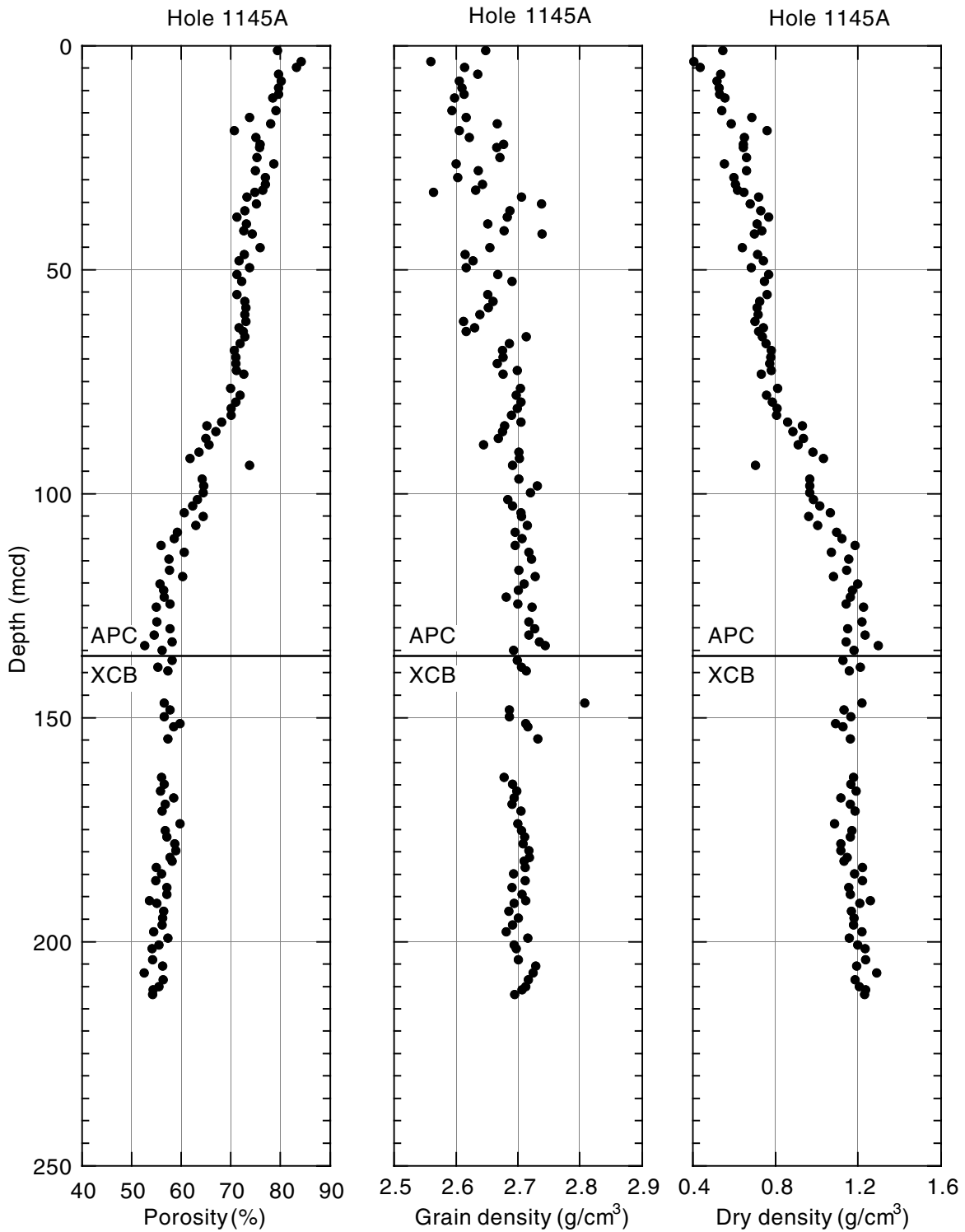
Figure F21. Color reflectance measurements from split-core surfaces at Site 1145 smoothed with a 20-point moving average. L*, a*, and b* are standard parameters calculated by the Minolta CM-2002 photospectrometer from the spectral data. L* = black line, a*/b* = gray line, APC = advanced hydraulic piston corer, XCB = extended core barrel.
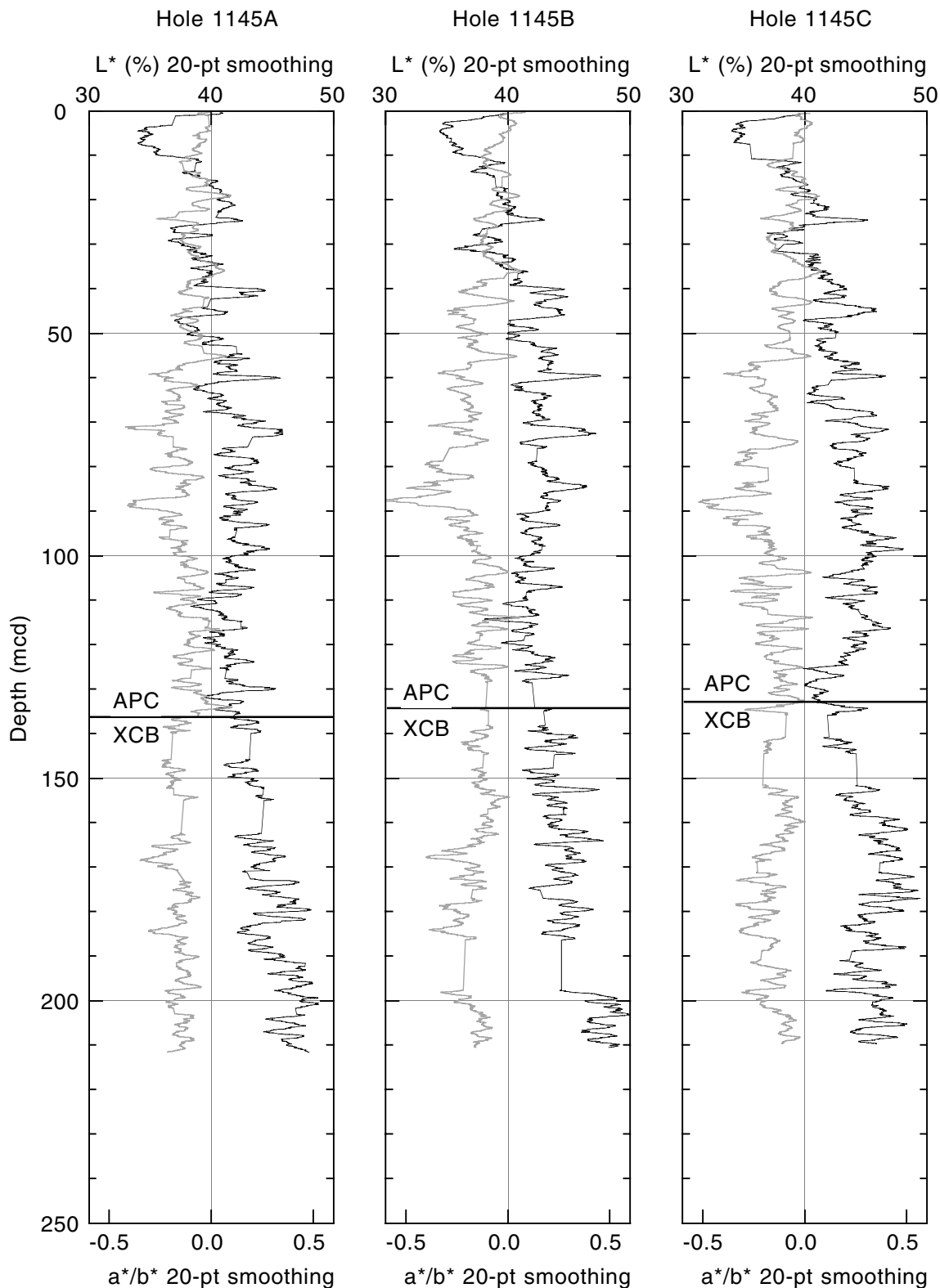
Figure F22. *P*-wave velocity measurements plotted for Hole 1145A. The offset at 58 mcd was caused by an operational error. Consequently, all PWS3 values below that depth were overestimated. For discussion of directional components, see "Physical Properties," p. 18, in the "Explanatory Notes" chapter.
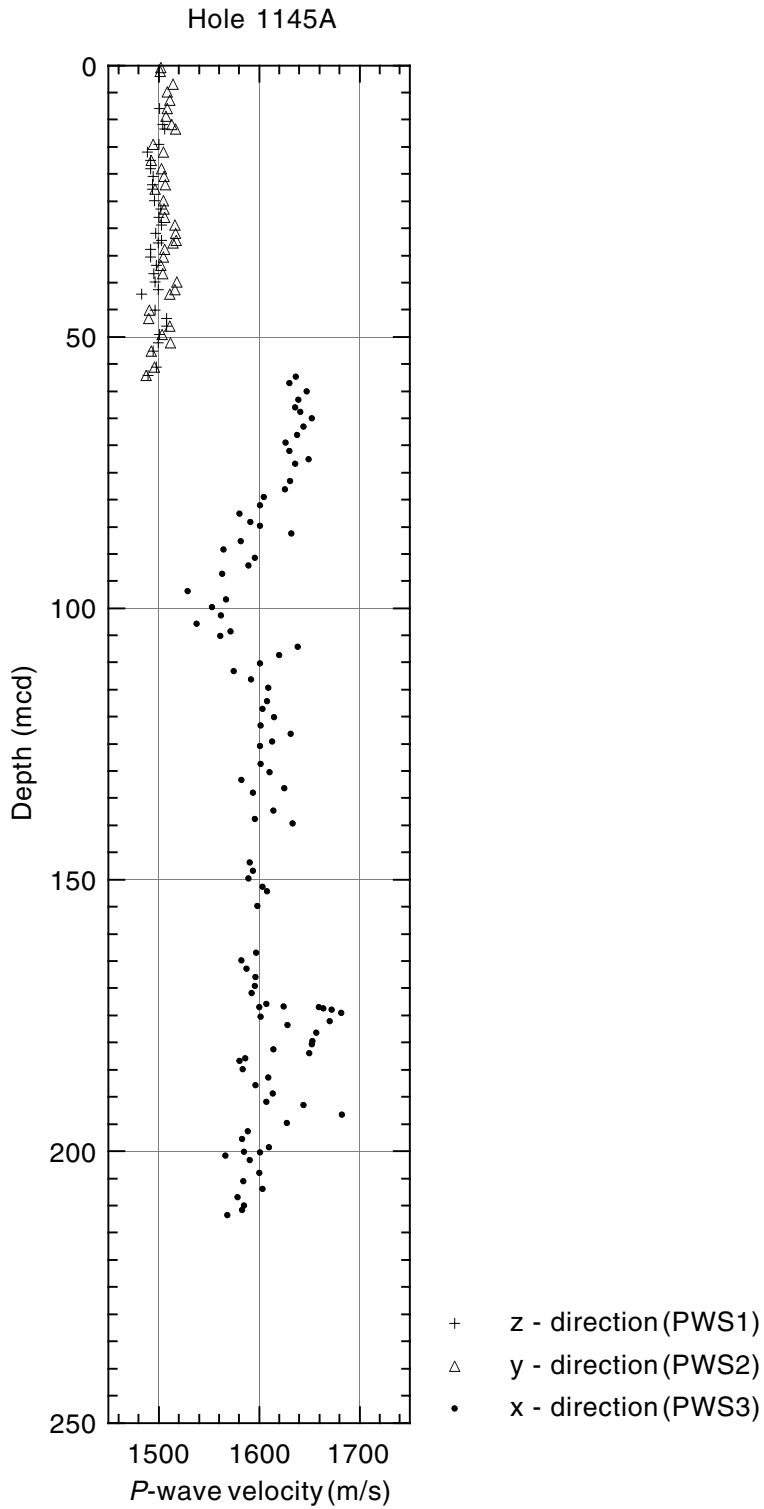
Figure F23. Thermal conductivity measurements for Hole 1145A. APC = advanced hydraulic piston corer, XCB = extended core barrel.
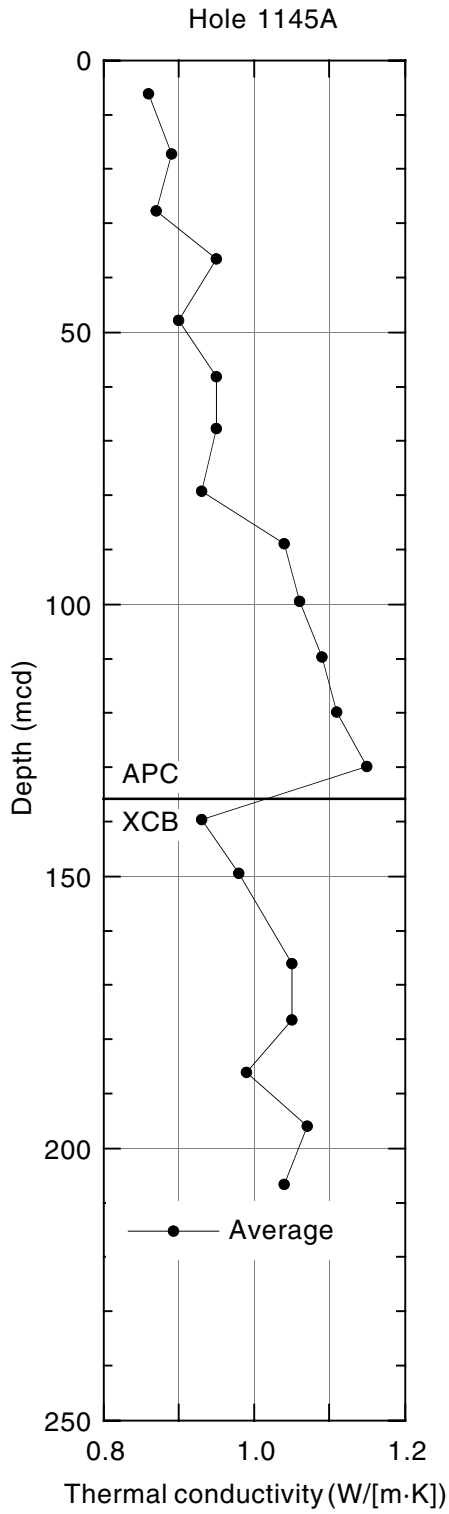
Figure F24. Downhole temperature measurements at Site 1145. **A.** Bottom-water temperature at Hole 1145B taken before Core 184-1145B-1H was shot. This value is taken as approximate bottom-water temperature at Site 1145. **B–D.** Downhole sediment temperature records and calculated equilibrium temperatures at Hole 1145A. Open circles = original temperature measurements, solid circles = selected section of data used in calculating the equilibrium temperature.
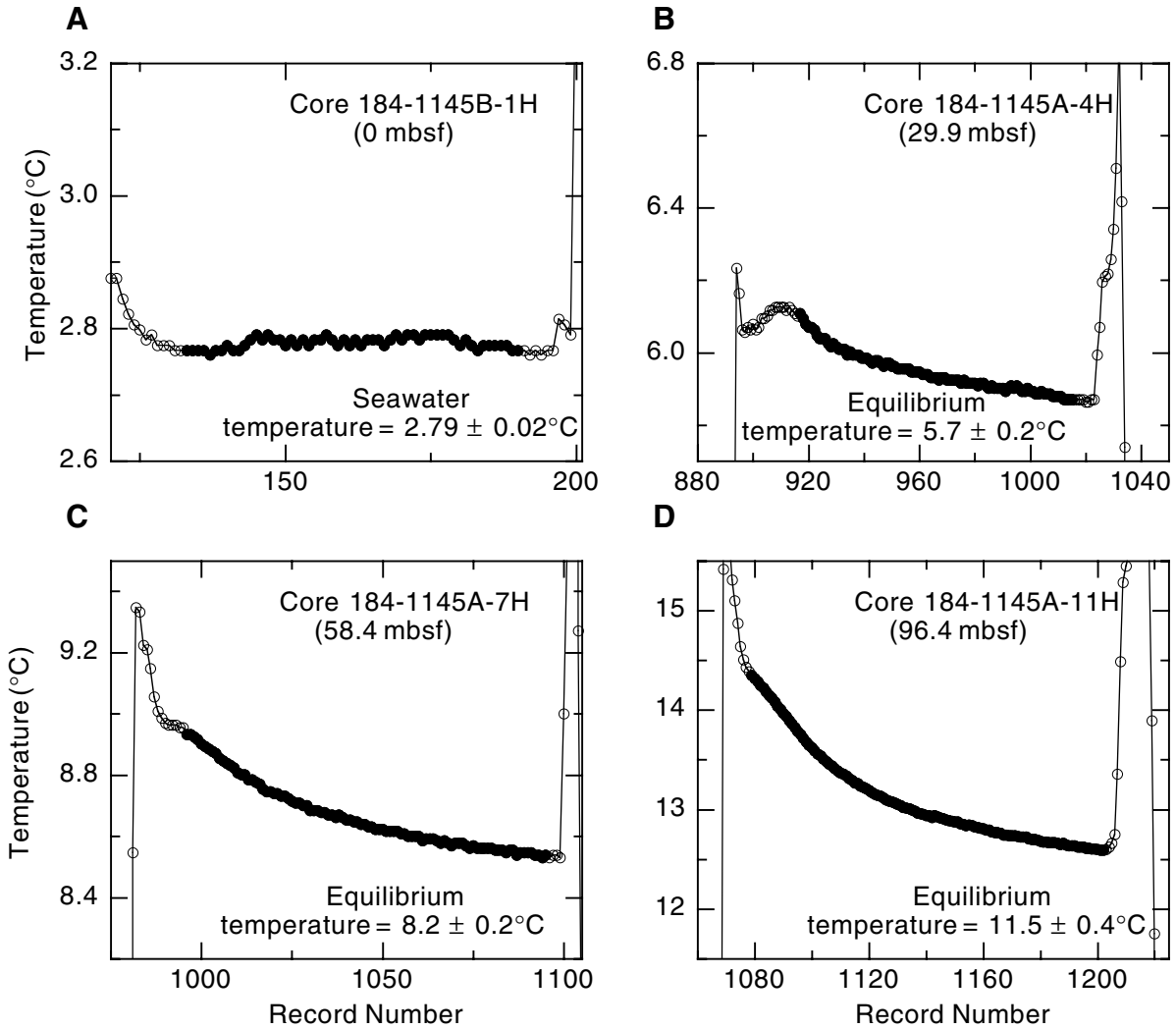
Figure F25. Downhole temperature gradient at Site 1145. T = temperature (°C) at depth (mbsf), R = correlation coefficient.

Plot with Temperature (°C) on the x-axis (0 to 20) and Depth (mbsf) on the y-axis (0 to 200).

$$T\ (°C) = 2.91 + 0.090 \times \text{depth (mbsf)}$$
$$R = 0.999$$
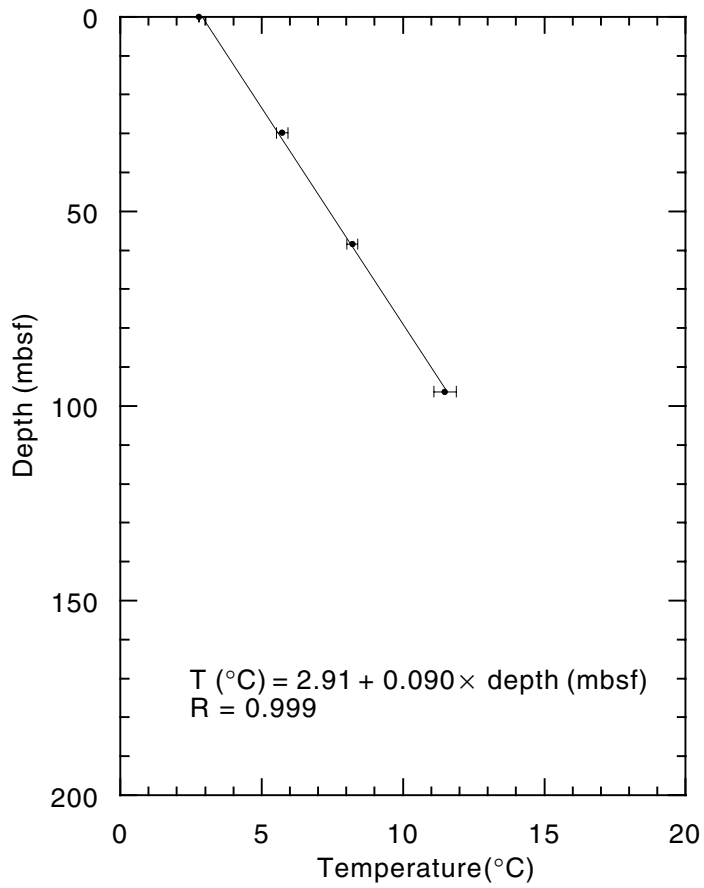
Table T1. Site 1145 coring summary. (**See table note.** Continued on next page.)

Core	Date (March 1999)	Time (UTC + 8 hr)	Depth Top (mbsf)	Depth Bottom (mbsf)	Depth Top (mcd)	Length (m) Cored	Length (m) Recovered	Recovery (%)
184-1145A-								
1H	19	0310	0.0	1.4	0.00	1.4	1.33	95.0
2H	19	0350	1.4	10.9	3.21	9.5	8.76	92.2
3H	19	0430	10.9	20.4	13.45	9.5	9.58	100.8
4H	19	0555	20.4	29.9	23.90	9.5	9.24	97.3
5H	19	0635	29.9	39.4	32.80	9.5	9.92	104.4
6H	19	0730	39.4	48.9	44.05	9.5	9.00	94.7
7H	19	0840	48.9	58.4	54.50	9.5	9.93	104.5
8H	19	0930	58.4	67.9	64.00	9.5	9.45	99.47
9H	19	1020	67.9	77.4	75.50	9.5	10.09	106.2
10H	19	1110	77.4	86.9	85.15	9.5	9.21	97.0
11H	19	1220	86.9	96.4	95.75	9.5	10.16	107.0
12H	19	1310	96.4	105.9	106.05	9.5	8.96	94.3
13H	19	1400	105.9	115.4	116.05	9.5	10.03	105.6
14H	19	1450	115.4	124.9	126.73	9.5	8.97	94.4
15X	19	1620	124.9	132.9	136.23	8.0	4.34	54.3
16X	19	1700	132.9	142.5	145.75	9.6	7.05	73.4
17X	19	1755	142.5	152.2	153.73	9.7	1.81	18.7
18X	19	1840	152.2	161.5	162.35	9.3	9.26	99.6
19X	19	1925	161.5	171.1	172.65	9.6	9.90	103.1
20X	19	2005	171.1	180.7	182.35	9.6	9.78	101.9
21X	19	2100	180.7	190.3	192.25	9.6	9.75	101.6
22X	19	2140	190.3	200.0	202.95	9.7	9.62	99.2
					Totals:	200.0	186.14	93.1
184-1145B-								
1H	20	0215	0.0	6.6	0.00	6.6	6.51	98.6
2H	20	0300	6.6	16.1	6.90	9.5	8.25	86.8
3H	20	0345	16.1	25.6	17.10	9.5	9.74	102.5
4H	20	0420	25.6	35.1	27.60	9.5	9.13	96.1
5H	20	0510	35.1	44.6	37.65	9.5	9.75	102.6
6H	20	0555	44.6	54.1	47.85	9.5	9.54	100.4
7H	20	0640	54.1	63.6	57.85	9.5	9.85	103.7
8H	20	0720	63.6	73.1	67.15	9.5	8.96	94.3
9H	20	0800	73.1	82.6	78.70	9.5	9.95	104.7
10H	20	0850	82.6	92.1	88.75	9.5	9.45	99.5
11H	20	0935	92.1	101.6	98.75	9.5	9.82	103.4
12H	20	1025	101.6	111.1	109.00	9.5	9.08	95.6
13H	20	1100	111.1	120.6	119.00	9.5	9.99	105.2
14X	20	1210	120.6	130.2	134.16	9.6	1.17	12.2
15X	20	1250	130.2	139.8	138.10	9.6	7.10	74.0
16X	20	1335	139.8	149.5	147.70	9.7	9.60	99.0
17X	20	1415	149.5	158.7	158.10	9.2	7.91	86.0
18X	20	1455	158.7	168.3	165.70	9.6	9.88	102.9
19X	20	1535	168.3	178.0	176.95	9.7	9.80	101.0
20X	20	1620	178.0	187.6	186.65	9.6	0.00	0.0
21X	20	1720	187.6	197.2	197.65	9.6	9.21	95.9
22X	20	1810	197.2	200.0	206.65	2.8	4.75	169.6
					Totals:	200.0	179.44	89.7
184-1145C-								
1H	20	2030	0.0	7.6	0.20	7.6	7.52	99.0
2H	20	2110	7.6	17.1	10.70	9.5	9.74	102.5
3H	20	2200	17.1	26.6	20.70	9.5	9.55	100.5
4H	20	2245	26.6	36.1	30.85	9.5	9.88	104.0
5H	20	2340	36.1	45.6	40.45	9.5	9.55	100.5
6H	21	0025	45.6	55.1	51.05	9.5	9.76	102.7
7H	21	0105	55.1	64.6	61.65	9.5	9.07	95.5
8H	21	0150	64.6	74.1	70.80	9.5	9.89	104.1
9H	21	0235	74.1	83.6	82.95	9.5	9.48	99.8
10H	21	0315	83.6	93.1	92.60	9.5	9.90	104.2
11H	21	0400	93.1	102.6	102.90	9.5	9.52	99.2
12H	21	0445	102.6	112.1	113.20	9.5	9.97	105.0
13H	21	0535	112.1	121.6	123.36	9.5	9.31	98.0
14X	21	0630	121.6	131.2	132.86	9.6	3.58	37.3
15X	21	0710	131.2	140.8	140.80	9.6	4.24	44.2

Table T1 (continued).

Core	Date (March 1999)	Time (UTC + 8 hr)	Depth Top (mbsf)	Depth Bottom (mbsf)	Depth Top (mcd)	Length (m) Cored	Length (m) Recovered	Recovery (%)
16X	21	0750	140.8	150.4	151.50	9.6	9.86	102.7
17X	21	0835	150.4	159.7	160.55	9.3	9.09	97.7
18X	21	0915	159.7	169.3	171.10	9.6	9.82	102.3
19X	21	1000	169.3	178.9	179.55	9.6	9.84	102.5
20X	21	1045	178.9	188.5	190.90	9.6	9.75	101.6
21X	21	1125	188.5	198.1	200.90	9.6	9.83	102.4
					Totals:	198.1	189.15	95.5

Notes: UTC = Universal Time Coordinated. This table is also available in **ASCII format.**

Table T2. Site 1145 coring summary by section.

Core	Date (March 1999)	Time (UTC + 8 hr)	Core depth (mbsf) Top	Core depth (mbsf) Bottom	Length (m) Cored	Length (m) Recovered	Recovery (%)	Section	Length (m) Liner	Length (m) Curated	Section depth (mbsf) Top	Section depth (mbsf) Bottom	Top depth (mcd)	Catwalk samples	Comments
184-1145A-															
1H	19	0310	0.0	1.4	1.4	1.33	95.0								
								1	1.20	1.20	0.00	1.20	0.00	HS	
								CC(w/1)	0.13	0.13	1.20	1.33	1.20	PAL	
								Totals:	1.33	1.33					
2H	19	0350	1.4	10.9	9.5	8.76	92.2								
								1	0.69	0.69	1.40	2.09	3.21		
								2	1.50	1.50	2.09	3.59	3.90		
								3	1.50	1.50	3.59	5.09	5.40	IW	
								4	1.50	1.50	5.09	6.59	6.90	HS	
								5	1.50	1.50	6.59	8.09	8.40		
								6	1.50	1.50	8.09	9.59	9.90		
								7	0.43	0.43	9.59	10.02	11.40		
								CC(w/7)	0.14	0.14	10.02	10.16	11.83	PAL	
								Totals:	8.76	8.76					
3H	19	0430	10.9	20.4	9.5	9.58	100.8								
								1	1.50	1.50	10.90	12.40	13.45		
								2	1.50	1.50	12.40	13.90	14.95		
								3	1.50	1.50	13.90	15.40	16.45	IW	
								4	1.50	1.50	15.40	16.90	17.95	HS	
								5	1.50	1.50	16.90	18.40	19.45		
								6	1.50	1.50	18.40	19.90	20.95		
								7	0.43	0.43	19.90	20.33	22.45		
								CC(w/7)	0.15	0.15	20.33	20.48	22.88	PAL	
								Totals:	9.58	9.58					
4H	19	0555	20.4	29.9	9.5	9.24	97.3								Adara; oriented
								1	1.50	1.50	20.40	21.90	23.90		
								2	1.50	1.50	21.90	23.40	25.40		
								3	1.50	1.50	23.40	24.90	26.90	IW	
								4	1.50	1.50	24.90	26.40	28.40	HS	
								5	1.50	1.50	26.40	27.90	29.90		
								6	1.00	1.00	27.90	28.90	31.40		
								7	0.66	0.66	28.90	29.56	32.40		
								CC(NS)	0.08	0.08	29.56	29.64	33.06	PAL	All to PAL
								Totals:	9.24	9.24					
5H	19	0635	29.9	39.4	9.5	10.12	106.5								Oriented
								1	1.50	1.50	29.90	31.40	32.80		
								2	1.50	1.50	31.40	32.90	34.30		
								3	1.50	1.50	32.90	34.40	35.80	IW	
								4	1.50	1.50	34.40	35.90	37.30	HS	
								5	1.50	1.50	35.90	37.40	38.80		

Notes: UTC = Universal Time Coordinated. The notation "CC(w/x)" refers to the D-tube in which the core catcher (CC) is stored, where x is the section number (1–7 or CC). NS = no section, HS = headspace, PAL = paleontology, IW = interstitial waters, SOLH = Solheid, MORA = Moran. Only a portion of this table appears here. The complete table is available in **ASCII format.**

Table T3. Site 1145 composite depths.

Core	Depth (mbsf)	Cumulative offset (m)	Depth (mcd)	Core	Depth (mbsf)	Cumulative offset (m)	Depth (mcd)
184-1145A-				12H	101.6	7.40	109.00
Continuous mcd:				13H	111.1	7.90	119.00
1H	0.0	0.00	0.00	14X	120.6	13.56	134.16
2H	1.4	1.81	3.21	Floating mcd:			
3H	10.9	2.55	13.45	15X	130.2	7.90	138.10
4H	20.4	3.50	23.90	16X	139.8	7.90	147.70
5H	29.9	2.90	32.80	17X	149.5	8.60	158.10
6H	39.4	4.65	44.05	18X	158.7	7.00	165.70
7H	48.9	5.60	54.50	19X	168.3	8.65	176.95
8H	58.4	5.60	64.00	20X	178.0	8.65	186.65
9H	67.9	7.60	75.50	21X	187.6	10.05	197.65
10H	77.4	7.75	85.15	22X	197.2	9.45	206.65
11H	86.9	8.85	95.75				
12H	96.4	9.65	106.05	184-1145C-			
13H	105.9	10.15	116.05	Continuous mcd:			
14H	115.4	11.33	126.73	1H	0.0	0.20	0.20
Floating mcd:				2H	7.6	3.10	10.70
15X	124.9	11.33	136.23	3H	17.1	3.60	20.70
16X	132.9	12.85	145.75	4H	26.6	4.25	30.85
17X	142.5	11.23	153.73	5H	36.1	4.35	40.45
18X	152.2	10.15	162.35	6H	45.6	5.45	51.05
19X	161.5	11.15	172.65	7H	55.1	6.55	61.65
20X	171.1	11.25	182.35	8H	64.6	6.20	70.80
21X	180.7	11.55	192.25	9H	74.1	8.85	82.95
22X	190.3	12.65	202.95	10H	83.6	9.00	92.60
				11H	93.1	9.80	102.90
184-1145B-				12H	102.6	10.60	113.20
Continuous mcd:				13H	112.1	11.26	123.36
1H	0.0	0.00	0.00	Floating mcd:			
2H	6.6	0.30	6.90	14X	121.6	11.26	132.86
3H	16.1	1.00	17.10	15X	131.2	9.60	140.80
4H	25.6	2.00	27.60	16X	140.8	10.70	151.50
5H	35.1	2.55	37.65	17X	150.4	10.15	160.55
6H	44.6	3.25	47.85	18X	159.7	11.40	171.10
7H	54.1	3.75	57.85	19X	169.3	10.25	179.55
8H	63.6	3.55	67.15	20X	178.9	12.00	190.90
9H	73.1	5.60	78.70	21X	188.5	12.40	200.90
10H	82.6	6.15	88.75				
11H	92.1	6.65	98.75				

Note: This table is also available in **ASCII format.**

Table T4. Site 1145 splice tie points.

Hole, core, section, interval (cm)	Depth (mbsf)	Depth (mcd)		Hole, core, section, interval (cm)	Depth (mbsf)	Depth (mcd)
Continuous splice:						
1145C-1H-1, 0	0.00	0.00				
1145C-1H-5, 82	6.82	7.02	Tie to	1145B-2H-1, 12	6.72	7.02
1145B-2H-5, 137	13.97	14.27	Tie to	1145C-2H-3, 57	11.17	14.27
1145C-2H-6, 82	15.92	19.02	Tie to	1145B-3H-2, 42	18.02	19.02
1145B-3H-6, 12	23.72	24.72	Tie to	1145A-4H-1, 82	21.22	24.72
1145A-4H-6, 52	28.42	31.92	Tie to	1145C-4H-1, 107	27.67	31.92
1145C-4H-7, 32	35.92	40.17	Tie to	1145B-5H-2, 102	37.62	40.17
1145B-5H-6, 113	43.73	46.28	Tie to	1145C-5H-4, 131	41.93	46.28
1145C-5H-6, 142	45.02	49.37	Tie to	1145B-6H-2, 1.5	46.12	49.37
1145B-6H-6, 138	53.48	56.73	Tie to	1145C-6H-4, 116	51.28	56.73
1145C-6H-6, 127	54.37	59.82	Tie to	1145B-7H-2, 46.5	56.07	59.82
1145B-7H-7, 8	63.18	66.93	Tie to	1145C-7H-4, 76	60.38	66.93
1145C-7H-5, 87	61.97	68.52	Tie to	1145B-8H-1, 136.5	64.97	68.52
1145B-8H-5, 42	70.02	73.57	Tie to	1145C-8H-2, 127	67.37	73.57
1145C-8H-4, 77	69.87	76.07	Tie to	1145A-9H-1, 57	68.47	76.07
1145A-9H-7, 37	77.27	84.87	Tie to	1145C-9H-2, 42	76.02	84.87
1145C-9H-5, 117	81.27	90.12	Tie to	1145B-10H-1, 137	83.97	90.12
1145B-10H-4, 58	87.68	93.83	Tie to	1145C-10H-1, 121	84.83	93.83
1145C-10H-7, 22	92.82	101.82	Tie to	1145B-11H-3, 7	95.17	101.82
1145B-11H-6, 142	101.02	107.67	Tie to	1145C-11H-4, 27	97.87	107.67
1145C-11H-7, 37	102.07	111.87	Tie to	1145B-12H-3, 17	104.47	111.87
1145B-12H-6, 122	110.02	117.42	Tie to	1145C-12H-3, 122	106.82	117.42
1145C-12H-6, 112	111.22	121.82	Tie to	1145B-13H-2, 132	113.92	121.82
1145B-13H-6, 107	119.72	127.62	Tie to	1145C-13H-3, 125.5	116.36	127.62
1145C-13H-7, 52	121.32	132.58				
Floating splice:						
1145B-16X-1, 0	139.80	147.70				
1145B-16X-5, 142	147.22	155.12	Tie to	1145C-16X-3, 59.5	144.42	155.12
1145C-16X-6, 77	149.07	159.77	Tie to	1145B-17X-2, 17	151.17	159.77
1145B-17X-5, 32	155.82	164.42	Tie to	1145C-17X-3, 87	154.27	164.42
1145C-17X-5, 72	157.12	167.27	Tie to	1145B-18X-2, 7	160.27	167.27
1145B-18X-6, 52	166.72	173.72	Tie to	1145C-18X-2, 112	162.32	173.72
1145C-18X-5, 142	167.12	178.52	Tie to	1145B-19X-2, 7	169.87	178.52
1145B-19X-6, 57	176.37	185.02	Tie to	1145A-20X-2, 117	173.77	185.02
1145A-20X-6, 122	179.82	191.07	Tie to	1145C-20X-1, 17	179.07	191.07
1145C-20X-6, 7	186.47	198.47	Tie to	1145B-21X-1, 82	188.42	198.47
1145B-21X-6, 28	195.38	205.43	Tie to	1145C-21X-4, 2.5	193.03	205.43
1145C-21X-7, 32	197.82	210.22				

Note: This table is also available in **ASCII format.**

Table T5. Intervals of lighter colored sediment in Hole 1145C.

Core, section, interval (cm)	Depth				Thickness (cm)
	Top		Bottom		
	(mbsf)	(mcd)	(mbsf)	(mcd)	
184-1145C-					
3H-3, 3-105	20.13	23.73	21.15	24.75	98
5H-4, 10-60	40.70	45.05	41.20	45.55	50
6H-6, 67-130	53.75	59.22	54.38	59.85	63
8H-1, 10, to 8H-2, 110	64.70	70.90	67.20	73.40	250
9H-2, 0-115	75.60	84.45	76.75	85.60	115
12H-2, 13-105	104.23	114.83	105.15	115.75	92
14X-2, 10-110	123.20	134.46	126.06	135.46	100
14X-3, 35, to 14X-CC, 53	124.65	135.91	125.18	136.44	53
14X-CC, 0-53	124.65	135.91	125.18	136.44	53
15X-2, 78-122	133.38	143.08	133.92	143.52	44
18X-2, 13, to 18X-3, 47	161.33	172.73	163.17	174.57	184
18X-4, 8-18	164.28	175.68	164.38	175.78	10
20X-2, 9-122	180.49	192.49	181.62	193.62	113
20X-3, 12-110	182.02	194.02	183.00	195.00	98
20X-4, 24-95	183.64	195.64	184.35	196.35	71

Table T6. Volcanic ash layers recovered at Site 1145.

Core, section, interval (cm)	Depth Top (mbsf)	Depth Top (mcd)	Depth Bottom (mbsf)	Depth Bottom (mcd)	Thickness (cm)	Remarks/Comments
184-1145A-						
11H-1, 7-9	86.97	95.82	86.99	95.84	2.0	Mostly quartz silt, maybe strongly altered
184-1145B-						
5H-1, 144-145	36.54	39.09	36.55	39.10	1.0	Dispersed ash layer
5H-6, 16-18	42.76	45.31	42.78	45.33	2.0	Light gray ash patches
8H-4, 50-53	68.60	72.15	68.63	72.18	3.0	Light gray ash patches
16X-6, 93-99	148.23	156.13	148.29	156.19	6.0	Nodular concretions of quartz silt, feldspars, and pyrite
184-1145C-						
6H-4, 86-91	50.96	56.41	51.01	56.46	5.0	Dispersed ash layer
16X-4, 25-29	145.55	156.25	145.59	156.29	4.0	Nodular concretions of quartz silt, feldspars, and pyrite

Table T7. Summary of biohorizons at Site 1145.

		Depth range of stratigraphic datums								
		Top			Bottom				Average	Average
Code	Events	Core, section, interval (cm)	Depth (mbsf)	Depth (mcd)	Core, section, interval (cm)	Depth (mbsf)	Depth (mcd)	Age (Ma)	depth (mcd)	sedimentation rate (m/m.y.)
		184-1145A-			184-1145A-					
CN	FO *E. huxleyi* acme	2H-CC, 9-14	10.11	**11.94**	3H-CC, 8-15	20.41	23.00	0.09	17.47	
PF	LO pink *G. ruber*	3H-CC, 8-15	20.41	23.00	4H-CC, 0-8	29.56	**33.11**	0.12	28.06	173
CN	FO *E. huxleyi*	6H-CC, 0-7	48.33	**53.20**	7H-CC, 36-43	58.76	64.40	0.26	58.80	
PF	FO pink *G. ruber*	8H-CC, 19-26	67.98	**73.62**	9H-CC, 29-36	77.92	85.56	0.40	79.59	
CN	LO *P. lacunosa**	8H-CC, 19-26	67.98	73.62	9H-CC, 29-36	77.92	**85.56**	0.46	79.59	
BF	LO *Stilostomella*	9H-CC, 29-36	77.92	85.56	10H-CC, 0-7	86.54	**94.33**	0.75	89.95	
CN	LO *C. macintyrei*	15X-CC, 54-59	129.19	140.54	16X-CC, 28-33	139.90	**152.77**	1.59	146.66	
PF	LO *G. fistulosus*	15X-CC, 54-59	129.19	140.54	16X-CC, 28-33	139.90	**152.77**	1.77	146.66	55
CN	LO *D. brouweri*	17X-CC, 44-49	144.26	155.51	18X-2, 100	154.70	**164.85**	1.95	160.18	
PF	FO *G. truncatulinoides*	17X-CC, 44-49	144.26	**155.51**	18X-CC, 31-36	161.41	171.58	2.00	163.55	
PF	LO *G. multicamerata**	19X-CC, 36-40	171.36	182.52	20X-CC, 46-50	180.84	**192.10**	2.4	187.31	
CN	LO *D. pentaradiatus*	19X-CC, 36-40	171.36	182.52	20X-CC, 46-50	180.84	**192.10**	2.52	187.31	
CN	LO *D. tamalis*	20X-CC, 46-50	180.84	192.10	21X-CC, 19-25	190.39	**201.97**	2.83	197.04	28
PF	LO *S. seminulina**	21X-CC, 19-25	190.39	201.97	22X-CC, 43-48	199.87	**212.54**	3.12	207.23	

Notes: Sources of reference age for all biostratigraphic events are listed in Tables T2, p. 42, and T3, p. 43, in the "Explanatory Notes" chapter. CN = calcareous nannofossils, PF = planktonic foraminifers, BF = benthic foraminifers, FO = first occurrence, LO = last occurrence. * = events used in calculating average sedimentation rates. Depth for the top and bottom of biostratigraphic events = the mean of the sample interval. Bars in average sedimentation rate column indicate the range of samples to which the average sedimentation rate applies. Depth in bold indicates where datum is recorded; depth range between the top and bottom is the interval where the real bioevent may occur.

Table T8. Calcareous nannofossil checklist for Site 1145.

Epoch	Zone (NN)	Zone (CN)	Core, section, interval (cm)	Depth (mcd)	Preservation	Abundance	Calcidiscus leptoporus	Calcidiscus macintyrei	Ceratolithus cristatus	Coccolithus pelagicus	Discoaster asymmetricus	Discoaster brouweri	Discoaster pentaradiatus	Discoaster quinqueramus	Discoaster surculus	Discoaster variabilis	Discosphaera tubifera	Emiliania huxleyi	Florisphaera profunda	Gephyrocapsa caribbeanica	Gephyrocapsa margarelii	Gephyrocapsa oceanica	Gephyrocapsa spp. (small)	Helicosphaera carteri	Helicosphaera hyalina	Helicosphaera inversa	Helicosphaera pavimentum	Helicosphaera wallichii	Oolithotus antillarum	Pontosphaera spp.	Pseudoemiliania lacunosa	Reticulofenestra asanoi	Reticulofenestra pseudoumbilicus	Reticulofenestra spp. (small-medium)	Rhabdosphaera clavigera	Scapholithus fossilis	Sphenolithus abies/neoabies	Syracosphaera pulchra	Syracosphaera spp.	Thorosphaera flabellata	Umbellosphaera irregularis	Umbellosphaera tenuis	Umbilicosphaera sibogae
Pleistocene	NN21b	CN15	184-1145A- 1H-CC, 8-13	1.25	A	G	C		R	R							R	D	A			A		F		R	R	F	R						F	C	F	F				R	F	C
			2H-CC, 9-14	11.89	A	G	F			R								D	A			A		F	F		R	F	R						F	R	F	R	R	R	R	R	F	C
			3H-CC, 8-15	22.93	C	M	F			R								C	A			C	F	F	R		R	F							F	R	F				R		C
	NN21a		4H-CC, 0-8	33.03	A	G	C			R								C	A	R		C	A	F			R	F						F	F	R	F	R			R	F	C
			5H-CC, 49-56	42.82	A	G	C			R								C	A	F	F	A	A	F	F	R	R	R	R	F	R			F	C	R	F			F	F		F
			6H-CC, 0-7	52.95	A	G	F			R	R							F	A	C	F	A	A	F				R	F					F	F	F	F				R		F
	NN20	CN13–14	7H-CC, 36-43	64.33	A	G	C			R									A	C	F	A	A	F	R	R	R	F	R	R			C	F	R	F	R	R	R			F
			8H-CC, 19-26	73.55	A	G	C				R								A	A	C	A	A	F		R	R	R					C	F	F	F		F	R			F
	NN19b		9H-CC, 29-36	85.49	A	G	C			R								D			A	A	F	F	R	F	R	F	R	C	F	R	F	R	C		F	F	R			C
			10H-CC, 0-7	94.26	C	P	F			R								A			C	C	R					F		R		F	R			R						F
			11H-CC, 42-48	105.82	C	M	F			R		R	R					A	C	F		F	C	R	R			R	A		R	R	F	F	R	R	R	R		R			R
			12H-CC, 14-20	114.92	C	P	F											C			F	F	R					A		R	R											
			13H-CC, 26-31	126.00	C	M	R	R	R			R	R					A			F	C	R					R	A		R	R	F			R					R	R
			14H-CC, 0-6	135.61	C	M	R			R								A			F	C	R					R	A				R	R			R			R			R
			15X-CC, 54-59	140.49	C	M	R			R								A		F	C	C	R					R	A				R	R		R		R			R			R
	NN19a		16X-CC, 28-33	152.72	A	M	F		C	R		R	R					A		F		A	F					F	A				F	C		R	F	R			R			R
			17X-CC, 44-49	155.46	A	M	F		F	R		R	R					C			D	F						F	A				F	F		F		F			R			R
late Pliocene	NN18	CN12d	18X-CC, 31-36	171.53	C	P	F		C	R		R				R	F			F								A		R	F				R							
	NN16–17	CN12a-c	19X-CC, 36-40	182.48	C	M			C	R	R	R		C	R		R	R		F								A		R	F		R	R					R	R		
			20X-CC, 46-50	192.06	A	M	R	C	F			C	C	A	F	R	R			C								A		R	C											
			21X-CC, 19-25	201.91	A	G	R	C	R	R		C	C	A		R	R	C					R					A		R	C											
			22X-CC, 43-48	212.49	C	P				R		C	C	A				C										A		R											C

Notes: D = dominant, A = abundant, C = common, F = few/frequent, R = rare, VG = very good, G = good, M = moderate, P = poor. See "Biostratigraphy," p. 9, in the "Explanatory Notes" chapter.

Table T9. Planktonic foraminifer checklist for Site 1145.

Epoch	Zone	Core, section, interval (cm)	Depth (mcd)	Abundance	Preservation	*Dentoglobigerina altispira*	*Globigerinoides extremus*	*Globorotalia crassaformis*	*Globorotalia tosaensis*	*Sphaeroidinellopsis seminulina*	*Globorotalia multicamerata*	*Sphaeroidinella dehiscens*	*Globigerinoides sacculifer*	*Neogloboquadrina dutertrei*	*Globigerinoides ruber*	*Globorotalia menardii*	*Globorotalia tumida*	*Globorotalia inflata*	*Globorotalia truncatulinoides*	*Pulleniatina obliquiloculata*	*Globigerinoides fistulosus*	*Globigerinoides conglobatus*	*Globigerinoides ruber* (pink)
Pleistocene	N22	184-1145A-																					
		1H-CC, 8-13	1.25	A	G							P	A	A	A	F		F	P	F		P	
		2H-CC, 9-14	11.89	A	G								F	F	A	F		A		F		R	
		3H-CC, 8-15	22.93	A	M							P	F	A	A	F		F	P	A		F	
		4H-CC, 0-8	33.03	A	G							P	R	F	A	R		F	P	F			P
		5H-CC, 49-56	42.82	A	G								R	F	A	R		F	R	F		R	P
		6H-CC, 0-7	52.95	A	G							P	R	F	A	R		F	F	R		R	P
		7H-CC, 36-43	64.33	A	G							P	R	R	A	R		F	P	R		R	P
		8H-CC, 19-26	73.55	A	M										A	F			P	A			
		9H-CC, 29-36	85.49	A	M								F		A			F	P	A			
		10H-CC, 0-7	94.26	A	G			P							F			A		F		R	
		11H-CC, 42-48	105.82	A	G			R				F			R	F		F		A			
		12H-CC, 14-20	114.92	C	M			P								A		F	R	F			
		13H-CC, 26-31	126.00	A	G			P								F		A	R	A			
		14H-CC, 0-6	135.61	A	G								F		A	F			P	A			
		15X-CC, 54-59	140.49	A	P						A					F			P	A			
		16X-CC, 28-33	152.72	A	G									A	A				F	R	R	F	
		17X-CC, 44-49	155.46	A	M							F	A	A				F	R	F			
late Pliocene	N21	18X-CC, 31-36	171.53	A	P				R			A							A				
		19X-CC, 36-40	182.48	A	P				R		P	A				R	R	F					
		20X-CC, 46-50	192.06	A	P						P	A	A	F									
		21X-CC, 19-25	201.91	A	P			P	F		R	A											
		22X-CC, 43-48	212.49	F	P	F	P	R	P	F													

Notes: D = dominant, A = abundant, C = common, F = few/frequent, R = rare, VG = very good, G = good, M = moderate, P = poor. See **"Biostratigraphy,"** p. 9, in the "Explanatory Notes" chapter.

Table T10. Age-depth relationship derived from the magnetic polarity time scale, Site 1145.

Polarity event	Age (Ma)	Depth (mcd) Hole 1145A	Depth (mcd) Hole 1145B	Depth (mcd) Hole 1145C	Average depth (mcd)
Brunhes/Matuyama	0.78	93.0	93.1	92.8	93.0
Upper Jaramillo	0.99	110.6	110.5	110.3	110.5
Lower Jaramillo	1.07	116.1	115.26	115.3	115.6
Upper Olduvai	1.77	154.6			154.6
Lower Olduvai	1.95	164.7			164.7
Matuyama/Gauss	2.58	190.0			190.0

Table T11. Sedimentation and accumulation rates for selected intervals, based on age-depth model and rates presented in Figure F14, p. 36.

	Bottom of interval		LSR total (m/m.y.)	LSR carbonate (m/m.y.)	MAR total (g/cm^2/k.y.)	MAR carbonate (g/cm^2/k.y.)
	Age (Ma)	Depth (mcd)				
NN21/NN20	0.26	57.8	227	23.0	14.7	1.51
Brunhes/Matuyama	0.78	93.0	80	7.5	6.4	0.60
Pleistocene/Pliocene	1.77	154.6	60	6.6	6.7	0.71
Bottom of hole	3.26	212.6	40	6.3	4.8	0.74

Note: LSR = linear sedimentation rate for total sediment and inorganic carbonate; MAR = mass accumulation rate for total sediment and inorganic carbonate.

Table T12. Inorganic carbon, carbonate, total carbon, total organic carbon, total nitrogen, and total sulfur contents at Site 1145.

Core, section, interval (cm)	Depth (mbsf)	Depth (mcd)	IC (wt%)	CaCO₃ (wt%)	TC (wt%)	TOC (wt%)	TN (wt%)	TS (wt%)	C/N
184-1145A-									
1H-1, 107-108	1.07	1.07	1.79	14.91	2.61	0.82	0.11	0.11	7.28
2H-1, 67-68	2.07	3.88	0.95	7.95					
2H-3, 107-108	4.66	6.47	1.13	9.43	2.16	1.03	0.13	0.21	7.94
2H-5, 107-108	7.66	9.47	1.05	8.75					
3H-1, 107-108	11.97	14.52	0.81	6.78					
3H-3, 107-108	14.97	17.52	1.44	12.02	2.20	0.76	0.11	0.23	6.94
3H-5, 107-108	17.97	20.52	0.90	7.50					
4H-1, 107-108	21.47	24.97	1.29	10.73					
4H-3, 107-108	24.47	27.97	1.10	9.14	1.95	0.85	0.11	0.27	7.84
4H-5, 107-108	27.47	30.97	0.83	6.91					
5H-1, 107-108	30.97	33.87	1.25	10.39					
5H-3, 107-108	33.97	36.87	1.67	13.89	2.57	0.90	0.12	0.36	7.34
5H-5, 107-108	36.97	39.87	2.10	17.51					
6H-1, 107-108	40.47	45.12	1.17	9.75					
6H-3, 107-108	43.47	48.12	1.67	13.94	2.47	0.79	0.10	0.21	8.09
6H-5, 107-108	46.47	51.12	1.01	8.40					
7H-1, 107-108	49.97	55.57	1.25	10.44					
7H-3, 107-108	52.97	58.57	0.77	6.40	1.32	0.55	0.09	0.29	6.39
7H-5, 107-108	55.97	61.57	2.03	16.92					
8H-1, 107-108	59.47	65.07	0.92	7.66					
8H-3, 107-108	62.47	68.07	1.02	8.47	1.66	0.65	0.09	0.22	7.60
8H-5, 107-108	65.47	71.07	0.58	4.79					
9H-1, 107-108	68.97	76.57	1.07	8.92					
9H-3, 107-108	71.97	79.57	1.39	11.62	1.95	0.56	0.08	0.15	6.61
9H-5, 107-108	74.97	82.57	1.11	9.25					
10H-1, 107-108	78.47	86.22	1.60	13.29					
10H-3, 107-108	81.47	89.22	1.19	9.93	1.70	0.51	0.08	0.10	6.41
10H-5, 107-108	84.47	92.22	0.73	6.05					
11H-1, 107-108	87.97	96.82	1.68	13.97					
11H-3, 107-108	90.97	99.82	1.57	13.08	2.16	0.59	0.08	0.24	7.54
11H-5, 107-108	93.97	102.82	1.47	12.27					
12H-1, 107-108	97.47	107.12	2.09	17.37					
12H-3, 107-108	100.47	110.12	0.39	3.23	0.73	0.34	0.07	0.05	5.23
12H-5, 107-108	103.47	113.12	1.61	13.39					
13H-1, 107-108	106.97	117.12	1.30	10.87					
13H-3, 107-108	109.97	120.12	0.70	5.84	1.03	0.33	0.07	<0.02	4.89
13H-5, 107-108	112.97	123.12	1.15	9.59					
14H-3, 107-108	118.85	130.18	1.34	11.17	1.57	0.23	0.06	<0.02	3.72
14H-5, 107-108	121.85	133.18	1.73	14.38					
15X-1, 107-108	125.97	137.30	1.22	10.14					
15X-3, 37-38	128.27	139.60	1.31	10.94	1.59	0.28	0.07	<0.02	4.20
16X-1, 107-108	133.97	146.82	1.40	11.62					
16X-3, 107-108	136.97	149.82	1.54	12.84	1.80	0.25	0.07	<0.02	3.52
16X-5, 64-65	139.54	152.39	2.22	18.52					
17X-1, 107-108	143.57	154.80	1.48	12.31	1.79	0.31	0.06	<0.02	4.98
18X-1, 107-108	153.27	163.42	1.06	8.82					
18X-3, 107-108	156.27	166.42	1.02	8.52	1.28	0.26	0.07	<0.02	3.72
18X-5, 107-108	159.27	169.42	1.74	14.51					
19X-1, 107-108	162.57	173.72	3.25	27.10					
19X-3, 107-108	165.57	176.72	2.10	17.53	2.35	0.24	0.06	0.03	4.06
19X-5, 107-108	168.57	179.72	2.85	23.73					
20X-1, 107-108	172.17	183.42	1.34	11.16					
20X-3, 107-108	175.17	186.42	2.29	19.07	2.55	0.26	0.07	<0.02	3.95
20X-5, 107-108	178.17	189.42	2.83	23.60					
21X-1, 107-108	181.77	193.32	3.66	30.46					
21X-3, 107-108	184.77	196.32	2.77	23.08	3.12	0.34	0.05	<0.02	6.63
21X-5, 107-108	187.77	199.32	2.80	23.32					
22X-1, 107-108	191.37	204.02	0.84	7.04					
22X-3, 107-108	194.37	207.02	1.50	12.48	1.80	0.30	0.06	<0.02	5.49
22X-5, 107-108	197.37	210.02	1.39	11.60					

Note: IC = inorganic carbon, CaCO₃= carbonate, TC = total carbon, TOC = total organic carbon, TN = total nitrogen, TS = total sulfur, C/N = carbon/nitrogen ratio.

Table T13. Rock-Eval pyrolysis results for Site 1145.

Core, section, interval (cm)	Depth (mbsf)	Depth (mcd)	T_{max}	S_1	S_2	S_3	TOC	PI	HI	OI
184-1145A-										
1H-1, 107-108	1.07	1.07	390	0.13	0.49	2.14	0.46	0.21	106	465
2H-3, 107-108	4.66	6.47	397	0.15	0.70	2.14	0.84	0.18	83	254
3H-3, 107-108	14.97	17.52	390	0.12	0.51	2.13	0.51	0.19	100	417
5H-3, 107-108	33.97	36.87	393	0.15	0.70	2.15	0.67	0.18	104	320
6H-3, 107-108	43.47	48.12	395	0.13	0.55	1.96	0.58	0.19	94	337
8H-3, 107-108	62.47	68.07	383	0.07	0.31	1.64	0.42	0.18	73	390
12H-3, 107-108	100.47	110.12	464	0.02	0.13	0.65	0.23	0.14	56	282

Notes: T_{max} = temperature of maximum release of pyrolysis HC, S_1= mg/g volatile HC, S_2 = pyrolysis HC mg/g, S_3 = pyrolysis CO_2 mg/g, TOC = total organic carbon, PI = production index, HI = hydrogen index, OI = oxygen index. See **"Organic Geochemistry,"** p. 14, in the "Explanatory Notes" chapter, for more information.

Table T14. Composition of interstitial waters in Hole 1145A.

Core, section, interval (cm)	Depth (mbsf)	Depth (mcd)	pH	Alkalinity (mM)	Salinity	Cl^- (mM)	Na^+ (mM)	K^+ (mM)	Mg^{2+} (mM)	Ca^{2+} (mM)	SO_4^{2-} (mM)	HPO_4^{2-} (µM)	NH_4^+ (mM)	H_4SiO_4 (µM)	Li^+ (µM)	S^{2+} (µM)
184-1145A-																
2H-3, 145-150	5.07	6.85	7.5	9.1	34.0	553	474	11.4	51.2	10.0	23.3	43.2	0.7	651	21.5	82.5
3H-3, 145-150	15.38	17.90	7.5	16.1	34.0	559	481	11.5	49.6	6.6	16.0	101.4	1.7	687	21.0	77.6
4H-3, 145-150	24.88	28.35	7.5	19.8	34.0	560	478	11.5	48.7	5.6	10.4	92.8	2.0	846	23.0	74.2
5H-3, 145-150	34.38	37.25	7.3	21.3	33.0	560	480	11.1	47.2	4.9	8.3	92.8	2.3	835	24.0	73.8
6H-3, 145-150	43.88	48.50	7.3	21.3	33.0	560	479	10.7	46.7	4.6	7.0	72.3	2.5	878	26.0	74.8
7H-3, 145-150	53.38	58.95	7.5	21.3	33.0	563	479	12.7	45.6	4.6	5.4	63.7	2.3	900	30.0	74.8
8H-3, 145-150	62.88	68.45	7.3	20.5	33.0	561	482	10.4	43.9	4.9	5.4	51.7	2.3	905	33.0	78.5
9H-3, 145-150	72.38	79.95	7.3	18.8	33.0	560	479	9.8	43.6	5.2	5.0	39.7	2.1	916	37.0	79.5
12H-3, 145-150	100.88	110.50	7.6	14.0	33.0	560	484	8.7	40.3	4.5	5.0	7.7	1.6	276	30.5	114.1
15X-2, 145-150	127.88	139.18	7.6	9.6	33.0	562	486	7.4	39.4	5.2	6.2	2.8	1.4	220	27.0	135.4
18X-3, 145-150	156.68	166.80	7.4	6.9	32.0	562	487	6.3	37.9	5.9	7.4	0.9	1.4	249	30.0	192.6
21X-3, 145-150	185.18	196.70	7.4	5.1	32.0	559	480	5.7	37.6	8.0	7.5	0.5	1.2	274	32.8	272.1

Table T15. Thermal conductivity measurements at Site 1145.

Leg	Site	Hole	Core	Type	Section	Top	Bottom	(mbsf)	(mcd)	(W/[m·K])	Average
184	1145	A	2	H	3	75	75	4.34	6.15	0.846	
184	1145	A	2	H	3	75	75	4.34	6.15	0.887	
184	1145	A	2	H	3	75	75	4.34	6.15	0.854	0.86
184	1145	A	3	H	3	75	75	14.65	17.20	0.859	
184	1145	A	3	H	3	75	75	14.65	17.20	0.900	
184	1145	A	3	H	3	75	75	14.65	17.20	0.898	0.89
184	1145	A	4	H	3	75	75	24.15	27.65	0.858	
184	1145	A	4	H	3	75	75	24.15	27.65	0.880	
184	1145	A	4	H	3	75	75	24.15	27.65	0.861	0.87
184	1145	A	5	H	3	75	75	33.65	36.55	0.982	
184	1145	A	5	H	3	75	75	33.65	36.55	0.924	
184	1145	A	5	H	3	75	75	33.65	36.55	0.936	0.95
184	1145	A	6	H	3	75	75	43.15	47.80	0.911	
184	1145	A	6	H	3	75	75	43.15	47.80	0.895	
184	1145	A	6	H	3	75	75	43.15	47.80	0.881	0.9
184	1145	A	7	H	3	75	75	52.65	58.25	0.922	
184	1145	A	7	H	3	75	75	52.65	58.25	0.966	
184	1145	A	7	H	3	75	75	52.65	58.25	0.955	0.95
184	1145	A	8	H	3	72	72	62.12	67.72	0.951	
184	1145	A	8	H	3	72	72	62.12	67.72	0.959	
184	1145	A	8	H	3	72	72	62.12	67.72	0.953	0.95
184	1145	A	9	H	3	75	75	71.65	79.25	0.930	
184	1145	A	9	H	3	75	75	71.65	79.25	0.924	
184	1145	A	9	H	3	75	75	71.65	79.25	0.935	0.93
184	1145	A	10	H	3	75	75	81.15	88.90	1.056	
184	1145	A	10	H	3	75	75	81.15	88.90	1.021	
184	1145	A	10	H	3	75	75	81.15	88.90	1.054	1.04
184	1145	A	11	H	3	75	75	90.65	99.50	1.058	
184	1145	A	11	H	3	75	75	90.65	99.50	1.054	
184	1145	A	11	H	3	75	75	90.65	99.50	1.081	1.06
184	1145	A	12	H	3	73	73	100.13	109.78	1.104	
184	1145	A	12	H	3	73	73	100.13	109.78	1.072	
184	1145	A	12	H	3	73	73	100.13	109.78	1.107	1.09
184	1145	A	13	H	3	79	79	109.69	119.84	1.097	
184	1145	A	13	H	3	79	79	109.69	119.84	1.131	
184	1145	A	13	H	3	79	79	109.69	119.84	1.114	1.11
184	1145	A	14	H	3	75	75	118.53	129.86	1.158	
184	1145	A	14	H	3	75	75	118.53	129.86	1.135	
184	1145	A	14	H	3	75	75	118.53	129.86	1.166	1.15
184	1145	A	15	X	3	38	38	128.28	139.61	0.927	
184	1145	A	15	X	3	38	38	128.28	139.61	0.928	
184	1145	A	15	X	3	38	38	128.28	139.61	0.930	0.93
184	1145	A	16	X	3	75	75	136.65	149.50	0.982	
184	1145	A	16	X	3	75	75	136.65	149.50	0.967	
184	1145	A	16	X	3	75	75	136.65	149.50	0.991	0.98
184	1145	A	18	X	3	72	72	155.92	166.07	1.079	
184	1145	A	18	X	3	72	72	155.92	166.07	1.054	
184	1145	A	18	X	3	72	72	155.92	166.07	1.020	1.05
184	1145	A	19	X	3	75	75	165.25	176.40	1.049	
184	1145	A	19	X	3	75	75	165.25	176.40	1.041	
184	1145	A	19	X	3	75	75	165.25	176.40	1.068	1.05
184	1145	A	20	X	3	75	75	174.85	186.10	1.000	
184	1145	A	20	X	3	75	75	174.85	186.10	0.990	
184	1145	A	20	X	3	75	75	174.85	186.10	0.989	0.99
184	1145	A	21	X	3	75	75	184.45	196.00	1.070	
184	1145	A	21	X	3	75	75	184.45	196.00	1.063	
184	1145	A	21	X	3	75	75	184.45	196.00	1.062	1.07
184	1145	A	22	X	3	75	75	194.05	206.70	1.096	
184	1145	A	22	X	3	75	75	194.05	206.70	1.009	
184	1145	A	22	X	3	75	75	194.05	206.70	1.013	1.04

Note: This table is also available in **ASCII format.**